



**21 Abstract (248 words)**

22 Graphite is considered as a material that promotes fault weakening and electrical  
23 conductivity ( $\sigma$ ) enhancement at fault zones. We studied how shear deformation may affect the  
24 evolution of friction and electrical conductivity of synthetic quartz (Qz)-graphite (Gr) mixtures  
25 and, more importantly, whether the  $\sigma$  of the mixtures present visible changes at the beginning of  
26 the simulated fault slip. Long-displacement friction experiments were performed on 1.2–2.3 mm-  
27 thick gouge specimens of varied Gr volume fraction ( $X_{Gr} = 0\text{--}100$  vol.%) under identical normal  
28 stress (2 or 5 MPa), slip rate ( $\sim 1.0$  mm/s), and  $N_2$ -flushing conditions. The experimental results  
29 suggested that the  $\sigma$  of the specimens with  $\geq 4.6$  vol.%  $X_{Gr}$  abruptly increased under limited shear  
30 displacement. With continued shear, the steady-state electrical conductivity ( $\sigma_{ss}$ ) increased by  
31 more than seven orders of magnitude when  $X_{Gr} > 3.4$  vol.%, while the steady-state frictional  
32 coefficient remained high (0.54–0.80) except for the specimens with  $X_G > 13.6$  vol.%. The post-  
33 mortem microstructures revealed that the high  $\sigma_{ss}$  observed in the intermediate Gr content  
34 specimens (3.4–13.6 vol.%) is associated with an *ad-hoc* fabric (graphite–cortex clasts) present  
35 in the principal slip zone. For high Gr content, excess Gr flakes fill the pores and help develop  
36 mechanically lubricated surfaces. We propose that low Gr content (i.e., as low as 3.4 vol.%) can  
37 cause high conductivity anomalies in natural shear zones. Overall, the findings suggest that the  
38 initiation of slips within carbonaceous shear zones can be detected by identifying unusual  
39 temporal signals using electromagnetic stations.

40

**41 Plain Language Summary (172 words)**

42 Crystalline graphite (Gr) can be enriched within fault zones due to mechanical or chemical  
43 processes and is considered a material that promotes fault weakening and electrical conductivity  
44 enhancement at fault zones. Geophysical observations suggest highly conductive anomalies in  
45 the carbonaceous shear zones and low apparent resistivity anomalies prior to an earthquake.  
46 Given this, we designed a novel experimental assembly to conduct electrical conductivity  
47 measurements on Gr-bearing fault rocks along a fault-parallel direction during a progressive fault  
48 slip in the laboratory. Our results revealed notably enhanced electrical conductivity under limited  
49 shear displacement, corresponding to the beginning of the simulated fault slip. With continued  
50 shear, the steady-state electrical conductivity increases by more than seven orders of magnitude

51 as the Gr content exceeds 3.4 vol.%, while the steady-state frictional coefficient remains high  
52 until the Gr content exceeds 13.6 vol.%. Our results demonstrate that interconnected Gr networks  
53 are one of the main mechanisms that can explain high conductivity anomalies at shear zones and  
54 facilitate the detection of initiated slips in carbonaceous shear zones using electromagnetic  
55 stations.

56

## 57 **1. Introduction**

58 Foliated fault rocks with anastomosing-network fabric composed of weak minerals (mostly  
59 phyllosilicate or carbonaceous materials [CMs]) are widely reported at natural fault zones (e.g.,  
60 Collettini et al., 2009; Collettini et al., 2019; Kuo et al., 2022; Manatschal, 1999; Oohashi et al.,  
61 2012). As revealed by their surface outcrops, CMs are present in several shear zones, especially  
62 in deep ductile shear bands (e.g., Kedar et al., 2020; Lyu et al., 2020; Nakamura et al., 2015;  
63 Puelles et al., 2014; Rawat & Sharma, 2011). Recent studies also report that CMs are  
64 occasionally locally present in shallow brittle fault zones, such as in coseismic surface ruptures  
65 (e.g., Kouketsu et al., 2017; Oohashi et al., 2012; Togo et al., 2011) or in drilling boreholes  
66 across principal slip zones (e.g., Chen et al., 2016; Hirono et al., 2009; Kirilova et al., 2018b;  
67 Kuo et al., 2014; Zulauf et al., 1999). The fraction of CMs varies among carbonaceous fault  
68 zones. Most fault gouges contain ~1–36% CMs (Chen et al., 2017; Chen et al., 2016; Nakamura  
69 et al., 2015; Wang et al., 2014). Some contain even 2–12 wt.% of crystalline graphite (Gr), a  
70 special member of CMs (Manatschal, 1999; Oohashi et al., 2012). Due to diffusive mass transfer  
71 or fluid precipitation during faulting, CMs can progressively become enriched toward the center  
72 of fault zones (i.e., the principal slip zones) to accommodate large shear deformation (Kuo et al.,  
73 2014; Oohashi et al., 2012; Oohashi et al., 2013). Moreover, Gr-bearing shear zones show low  
74 electrical resistivity in magnetotelluric (MT) surveys, generally in the range of 0.100–0.005 S/m  
75 (e.g., Pous et al., 2004; Ritter et al., 2005; Wannamaker et al., 2002; Zhao et al., 2012).

76 Mechanical tests on binary (or ternary) mixtures of hard and weak minerals show that the  
77 shear strength of mixtures monotonically decreases with increasing content of weak minerals  
78 (Crawford et al., 2008; Moore & Lockner, 2011; Takahashi et al., 2007; Tembe et al., 2010). In  
79 particular, highly crystalline Gr has been characterized as a "dry" solid lubricant of fault zones  
80 because of its sheet structure held together solely by van der Waals forces (Kirilova et al., 2018a;

81 Moore & Lockner, 2004). Previous studies have shown that the steady-state frictional coefficient  
82 of Gr can remain at very low values (between  $\sim 0.1$  and  $\sim 0.2$ ) over a wide range of slip rates  
83 ( $5 \times 10^{-4}$ – $1.3$  m/s) (Kirilova et al., 2018a; Oohashi et al., 2011; 2013). Even a small amount of Gr  
84 ( $\sim 10$  vol.%) in a fault gouge can mechanically smear on the principal shear plane. It makes fault  
85 rocks dramatically weaker than expected when considering Byerlee's law (0.6–0.85 in friction  
86 coefficient, Byerlee, 1978; Oohashi et al., 2013; Rutter et al., 2013).

87 Grain-boundary Gr films (a few ppm), with thicknesses ranging from a few to several tens  
88 of nanometers, can produce highly interconnected conductive networks. Their electrical  
89 conductivity reaches 0.005–0.010 S/m (Duba & Shankland, 1982; Frost et al., 1989; Glover &  
90 Vine, 1992; Mareschal et al., 1992). Such films may exist in the range of crustal depth (Selway,  
91 2013). They have been considered as a potential mechanism explaining high conductivity  
92 anomalies in crustal shear zones (Chen et al., 2017; Glover & Ádám, 2008; Haak et al., 1997;  
93 Monteiro Santos et al., 2002). Moreover, apparent resistivity anomalies prior to an earthquake  
94 (typically descending by 1~7%) detected by electromagnetic stations have been considered as a  
95 precursor factor in medium- or short-term earthquake prediction (e.g., Du, 2011; Honkura et al.,  
96 2013; Lu et al., 2016; Madden et al., 1993; Zhao & Qian, 1994) despite their strong spatial  
97 anisotropy. Nover et al. (2005) showed that shearing deformation can enhance the electrical  
98 conductivity of carbon-bearing rocks by about three orders of magnitude. Glover & Ádám (2008)  
99 attributed this enhancement to the smearing effect and proposed that this effect can explain many  
100 precursory and coseismic geoelectric phenomena observed in nature (Mathez et al., 2008;  
101 Roberts et al., 1999). However, to date, there are insufficient systematic real-time observations of  
102 the mechanical and electrical characteristics of shearing carbon-bearing gouges. It leads to  
103 incomplete theoretical support for explaining the origin of high conductivity anomalies in deep  
104 shear zones and effectively obtaining the frictional slip information in shallow fault zones.

105 In this study, we used a rotary shear apparatus to conduct continuous electrical conductivity  
106 measurements on controlled-dry, synthetic, Gr-bearing gouges along the fault-parallel direction  
107 during progressive fault slip. The experiments were conducted at fixed velocity ( $\sim 1$  mm/s),  
108 normal stress (2 or 5 MPa), and under ambient temperature,  $N_2$  atmosphere conditions. Results  
109 showed that an increasing Gr content can effectively reduce the frictional strength, while an  
110 initial very limited shear displacement causes an abrupt enhancement of the electrical

111 conductivity. We further investigated the microstructure evolution of specimens with different Gr  
112 contents and found that the high electrical conductivity observed might be related to the  
113 development of Gr flakes on the grain boundaries. Our work gives insights into the coupling  
114 effect between frictional strength and electrical conductivity of Gr-bearing fault zones.  
115 Additionally, it offers experimental evidence for detecting initiated slips using electromagnetic  
116 approaches.

117

## 118 **2. Materials and methods**

### 119 **2.1. Starting materials**

120 The starting materials used in our experiments were commercial Gr powders (Xilong  
121 Scientific Co., Ltd., analytical grade, > 98.5% purity, Figure S1a in Supporting Information) and  
122 Quartz (Qz) particles (collected from Fengyang County, Anhui Province, China P.R., > 99.3%  
123 purity, Figure S1b in Supporting Information). The sizes of the Qz particles were determined by  
124 laser diffraction analysis (Microtrac S3500), which resulted in a median diameter of 12.2  $\mu\text{m}$  and  
125 a size distribution comparable to that of natural fault gouges (Chen et al., 2017) (Figure S1c in  
126 Supporting Information). Synthetic fault gouges were prepared by mixing the Qz particles with  
127 Gr powders in contents of 0, 3, 4, 5, 6, 9, 10, 12, 15, 25, 50, and 100 wt.%. According to the  
128 particle densities (2.31  $\text{g}/\text{cm}^3$  for Gr and 2.66  $\text{g}/\text{cm}^3$  for Qz) measured by the true density  
129 analyzer (AccuPyc II 1340, errors  $\pm 0.03\%$ ), the estimated volumetric percentages of Gr in the  
130 mixtures were 0.0, 3.4, 4.6, 5.7, 6.8, 10.2, 11.3, 13.6, 16.9, 27.7, 53.5 and 100 vol.%, respectively.

131

### 132 **2.2 Experimental assembly adapted to friction–conductivity measurements**

133 The experiments were conducted using the low- to high-velocity rotary shear apparatus  
134 installed at the Institute of Geology, China Earthquake Administration (IGCEA) (Figures 1a–1c).  
135 For this instrument, the variation of axial force (i.e., normal stress) could be controlled within 2–  
136 3%, the resolution of shear displacement is  $\sim 30 \mu\text{m}$ , and the accuracy of the measured shear  
137 torque is greater than 99% (Ma et al., 2014). We adapted a ring-shear setup for gouge-type  
138 friction experiments to monitor the transient electrical conductivity (real-time response of the  
139 electrical conductivity,  $\sigma$ ) of simulated faults (Figure 1d) in their fault-parallel direction (Figure

140 1e). For testing the assembly, a simulated gouge layer with ~2.0 mm thickness was uniformly  
141 placed between a pair of 40 mm-long corundum hollow cylinders with an inner diameter ( $l_i$ ) of  
142 28 mm and an outer diameter ( $l_o$ ) of 40 mm, respectively. In previous experiments that used the  
143 ring-shaped assembly, before our adaptation, the gouge layer was typically confined by the  
144 tightly fitted outer and inner Teflon<sup>®</sup> sleeve/cylinder to minimize gouge extrusion (e.g., Boulton  
145 et al., 2017; Hou et al., 2012; Yao et al., 2013a; Yao et al., 2013b). However, in the designed  
146 setup, to allow the electrical conductivity measurement, two titanium-alloy electrodes (a loop  
147 and a centered vertical cylinder) were embedded into the outer Teflon<sup>®</sup> sleeve and inner cylinder,  
148 respectively (Chen, 2022; Han et al., 2019). To avoid direct contact between the upper (rotary)  
149 corundum cylinder and the electrodes, the gap between them was kept at ~100  $\mu\text{m}$ . We note that  
150 a small quantity of gouge was expected to extrude into the gaps during the experiments. It could  
151 presumably cause some uncertainty in the friction data. One or two lead wires led respectively  
152 from the two stainless steel screws on the two electrodes (Figure 1b). They were connected to the  
153 Keithley instruments (Tektronix Company, U.S.) used to measure the electrical resistance ( $R_E$ ).  
154 In addition, a suit of elastomers fixed the three-layered outer sleeve to the lower corundum  
155 cylinder. Finally, to achieve a dry and anoxic environment, the whole assembly was enclosed by  
156 a transparent polymethylmethacrylate (PMMA) vessel. A (high purity)  $\text{N}_2$  atmosphere was  
157 maintained inside the vessel during the experiment.

158

### 159 2.3 Experimental procedure and data processing

160 A total of 19 experiments were performed on the different Gr–Qz mixtures under constant  
161 normal stresses ( $P_n = 2$  or 5 MPa) and room temperature conditions. The specimens were oven-  
162 dried at  $\geq 75$  °C for  $> 24$  h prior to the experiments. After setting up each specimen assembly, it  
163 was first compacted at the target  $P_n$  for 2–3 h and then sheared at a constant slip rate of 0.83–  
164 1.00 mm/s under dry conditions.

165 During the experiments, three Keithley instruments (6514 System Electrometer, 2182A  
166 Nanovoltmeter, and 6221 DC and AC Current Source) were used to measure  $R_E$ . These  
167 instruments are commercial products. They enable fast, precise, high-sensitivity measurements of  
168 various electrical parameters and have been widely used for constraining the electrical properties

169 of geological materials (e.g., Hou et al., 2021; Yamashita et al., 2014; Zhuang et al., 2021). As  
 170 the  $R_E$  values of our simulated specimens varied by almost 14 orders of magnitude (from 100 G $\Omega$   
 171 to 1 m $\Omega$ ), we used three different configurations and measurement modes depending on the  $R_E$   
 172 range. Thereby, the electrical potential ( $E$ ) and direct current ( $I$ ) [ $R_E = E/I$ , 4 wires setup] or  $R_E$  (2  
 173 wires setup) of the specimens were acquired. Details on the resistance measurement models and  
 174 corresponding measurement accuracies are presented in Table 1. The  $R_E$  values were obtained by  
 175 subtracting the background levels (0.0041  $\Omega$ ). They contained the electrical resistance of the  
 176 aluminum wires in the assembly and the Keithley instruments, which were assessed from the  
 177 electrode-to-electrode measurement. The  $\sigma$  values were calculated by taking the inverse of the  $R_E$   
 178 values and normalizing them with the scale as follows:

$$\sigma = \frac{\ln(I_o/I_i)}{2\pi\delta R_E} \quad (1)$$

179 where  $\delta$  is the thickness of the simulated gouge layer (mm). In some experiments, we paused the  
 180 motor for ~5 min to switch the measurement mode due to technical issues or unexpected changes  
 181 in  $\sigma$ . The consistency of the  $\sigma$  results between two modes demonstrates the relative accuracy of  
 182 our measurements.

183 Besides recording electrical data, the axial load, axial displacement, torque, and upper  
 184 piston rotation were also recorded at 20 Hz using a digital data recorder (KYOWA EDX-100A).  
 185 The raw data were processed to obtain  $P_n$ ,  $\delta$ , equivalent slip velocity ( $v_e$ , m/s), equivalent shear  
 186 stress ( $\tau$ , MPa), and apparent friction coefficient ( $\mu = \tau/\sigma_n$ ) vs shear displacement ( $D$ ) (Ma et al.,  
 187 2014). The  $\mu$  value was calculated after correcting the Teflon<sup>®</sup> friction (Hou et al., 2012). As  $R_E$   
 188 was also recorded at 20 Hz using the Keithley instruments, we carefully synchronized the two  
 189 recording systems by matching the feature points of  $R_E$ .

190 For quantitative comparison between the two quantities, we determined several critical  
 191 parameters from the  $\mu$  and  $\sigma$  vs  $D$  curves (Table 2, Figures 2–3). For instance,  $\mu_{ss}$  and  $\sigma_{ss}$  are the  
 192 nominal (quasi-) steady-state frictional coefficient and electrical conductivity achieved at long  
 193 displacement. They were obtained from the arithmetically average value of  $\mu$  in steady state and  
 194 the logarithmically average value of  $\sigma$  in steady state, respectively.  $D_{\mu ss}$  and  $D_{\sigma ss}$  are the  
 195 corresponding characteristic displacements. Moreover, we defined  $D_{\sigma ch}$  as the critical slip  
 196 displacement for abrupt electrical conductivity enhancement (i.e.,  $\sigma$ -jump phenomenon). Namely,

197 the  $\sigma$  curve, for the first time, shows an increase by more than one order of magnitude from the  
198 low initial level ( $\sigma_0 < 0.01$  S/m), or more than 1.5 times from a high initial level ( $\sigma_0 > 0.01$  S/m).  
199 For details on the data processing and determination of the critical parameters, we refer to Text  
200 S1 and Figure S2 in Supporting Information.

201 After the experiments, a scanning electron microscope (SEM, Zeiss Sigma-0380) was used  
202 to examine the microstructural developments as a function of the Gr content (Figure 1e). The  
203 scanning electron microscope was operated at an acceleration voltage of 15 kV in both the  
204 backscatter electron (BSE) and secondary electron (SE) modes. Microstructural images were  
205 taken from the corresponding Au-coated thin sections.

206

### 207 **3. Results**

208 The experimental data obtained from the 19 experiments (with the synthetic fault gouges)  
209 are presented in Table 2. As described in section 2.3, two series of data were obtained using our  
210 rotary-shear friction apparatus adapted for conducting transient electrical conductivity  
211 measurements.

212

#### 213 **3.1 General mechanical and electrical behaviors**

214 Figure 2 presents the mechanical (panels a–b) and electrical (panels c–d) behaviors of the  
215 Gr–Qz mixture specimens. They were sheared at a normal stress of 2 MPa as a function of slip  
216 displacement in both logarithmic (panels a and c) and linear (panels b and d) scales. With low to  
217 intermediate Gr contents ( $< 25$  wt.%), the specimens exhibited peak friction coefficients of 0.49–  
218 0.67 at less than 0.17 m slip displacement (Figure 2a). Then, it was followed by slip  
219 strengthening to  $\sim 1$  m and overall high friction levels (0.54–0.80) in the end (Figure 2b). With  
220 high Gr contents (25–50 wt.%), the peak friction reached 0.40–0.51 at a displacement of  $\sim 1$  mm,  
221 followed by dramatic slip weakening with steady-state friction coefficients of 0.10–0.19. At a  
222 high normal stress of 5 MPa, similar frictional behaviors were evident for both low and high Gr  
223 contents (Figure 3a).

224 The specimens showed large variations in electrical conductivity of up to 14 orders of  
225 magnitude (i.e., from  $10^{-11}$  to  $10^3$  S/m), depending on the Gr content and shear displacement. (1)

226 For Gr content < 4 wt.%,  $\sigma$  decreased slightly with initial shear displacement. (2) For Gr content  
 227 of 4–10 wt.%, the specimens showed intermediate  $\sigma_{ss}$  values in the range of  $10^{-3}$ –0.3 S/m.  
 228 Interestingly,  $\sigma$  increased remarkably with the slip progression after  $D_{\sigma ch}$  by more than six orders  
 229 of magnitude. (3) Specimens with Gr contents > 12 wt.% showed slight increases (a few times)  
 230 in  $\sigma$  with slip. The  $\sigma$  maintained high values (> 0.1 S/m) throughout the experiments.

231

### 232 3.2 Comparison of characteristic displacements

233 The results of the  $\sigma$ – $D$  and  $\mu$ – $D$  data by Gr content are presented in Figure 4. To reveal the  
 234 possible links between  $\sigma$  and  $\mu$ , we highlight the  $\sigma$  and  $\mu$  evolution at displacements between  $D_{\sigma ch}$   
 235 and  $D_{\sigma ss}$ , during which  $\sigma$  increased significantly.

236 The initial nearly-linear portions of the  $\mu$ – $D$  curves reflect the elastic shear loading  
 237 processes. Because the displacements in all  $\mu$ – $D$  and  $\sigma$ – $D$  plots are precisely the load point  
 238 displacements that embody the shear deformation of the entire testing system. The displacements  
 239 at which the  $\mu$ – $D$  curves deviate from straight lines are the starting points of the shear  
 240 deformation in the gouge layers (see the circle symbols in Figures 4d–4f, hereafter referred to as  
 241  $D_0$ ). Thus, the difference between  $D_0$  and  $D_{\sigma ch}$  represents the shear displacement required to  
 242 initiate the generation of a continuous electrically conductive layer associated with the shear  
 243 deformation of the Gr–Qz mixtures. Since the  $D_0$  values of all specimens are small and not very  
 244 different from one another (typically ~0.15–0.28 mm), we plotted  $D_{\sigma ch}$  against the Gr content in  
 245 Figure 4g and Figure 4h, while  $D_{\mu ss}$  and  $D_{\sigma ss}$  were plotted for comparison. As the Gr content  
 246 increased, the  $D_{\sigma ch}$  value decreased from 0.5 m, via 4 mm, to 0.2 mm; similarly,  $D_{\sigma ss}$  decreased  
 247 from 1.2 m, via 100 mm, to 3.0 mm. In contrast,  $D_{\mu ss}$  seemed to be independent of the Gr content,  
 248 thereby remaining at high values (mostly between 0.3 and 0.6 m). Therefore,  $D_{\sigma ch}$  and  $D_{\sigma ss}$  were  
 249 significantly lower than  $D_{\mu ss}$  at Gr content higher than ~9 wt.%. Consequently, for the mixtures  
 250 with 4–12 wt.% Gr, the critical slip displacement for the  $\sigma$  jump ( $D_{\sigma ch}$ ) was limited (as low as 0.2  
 251 mm) and smaller than the displacement for reaching the frictional steady state ( $D_{\mu ss}$ ) (see the start  
 252 of the bold curves in Figures 4d–4e). The  $\sigma$  jump occurred before the peak friction, even in the  
 253 case of mixtures with high Gr content (15–50 wt.%) (see the start of the bold curves in Figure 4f).

254

## 255           3.3 Microstructural evolution in steady state

256           As revealed by the BSE images of the epoxied post-mortem specimens, with increasing Gr  
257 content (0, 3, 9, and 25 wt.%), the specimens became increasingly cohesive after the experiment.  
258 The pure Qz gouge was the most fragile, showing a loose structure, whereas the high Gr content  
259 gouge layer could be recovered as an entire piece (Figure 5). A slickenside surface ornamenting  
260 the discrete shear surface of a high-Gr portion specimen was observed after the experiment  
261 (attached picture on top of Figure 5d), while a dark surface appeared on the surface of a low-Gr  
262 portion specimen (attached picture on top of Figure 5c).

263           The pure Qz gouge did not show a discernable strain localization zone (SLZ). However,  
264 discrete inclined openings were visible over the entire thickness, mostly along the Riedel shear  
265 (R shear, Logan et al., 1992), oriented at a low angle of  $10^{\circ}$ – $30^{\circ}$  to the shear direction (Figure  
266 5a). In contrast, remarkable shear bands were developed at the upper rotary boundaries in the  
267 other mixture specimens, especially those with low Gr contents (3 and 9 wt.%, Figures 5b and  
268 5c). In these two specimens, the angular fractured Qz particles of the lowest layer had relatively  
269 large grain sizes, similar to that of the pure Qz gouge (Layer III). The localized band was further  
270 divided into two layers (see the yellow dotted lines for the boundaries, Figures 5b and 5c).  
271 Generally, the middle layer was homogeneous, and its average grain size ( $\sim 5 \mu\text{m}$ ) was lower than  
272 that of the least deformed layer. The uppermost layer had the finest grain size, mostly lower than  
273  $\sim 1 \mu\text{m}$ . In a certain portion of this layer, agglomerated clumps of extremely fine Qz particles  
274 developed, characterized by thicknesses of  $\sim 10 \mu\text{m}$  and lengths varying from a few tens to a few  
275 hundreds of micrometers. Locally, they were cut by the R shear offset, manifested as discrete  
276 stripes parallel to the shear direction (Figures 5b and 5e). Such discrete clumps were interpreted  
277 as the migration of the microslip zone during extreme shearing deformation, in accordance with  
278 previous reports (Yao et al., 2013a; Yao et al., 2013b). The enlarged pictures indicate that these  
279 clumps were characterized by homogenous Qz grain size distribution and had extremely low  
280 porosity ( $< 5\%$ , estimated based on image analysis, Figure 5e), while the remainder of the upper  
281 layer had a broader grain size distribution (varying from 0.1 to  $1.0 \mu\text{m}$ ) and relatively high  
282 porosity (20–30%, Figure 5f). Gr flakes, with widths of up to several tens of nanometers, filled  
283 the space between the Qz particles to form anastomosing networks (Figure 5f). Consequently, the

284 microslip zone was developed from the middle layer and grew toward the upper boundary as the  
285 slip proceeded, as revealed by the comparison of the microstructures between Layers I and III.  
286 The microstructure of the high Gr specimen (25 wt.%) showed extremely localized deformation,  
287 and the shining surface on the specimen formed a 10–20  $\mu\text{m}$  layer (Figure 5d). The enlarged  
288 picture shows deflected Gr flakes that formed anastomosing networks around broken Qz  
289 particles.

290 The Gr and the epoxy resin were difficult to distinguish at the submicron scale based on  
291 SEM images. Thus, we directly observed the unepoxied specimens of 12 wt.% Gr-bearing  
292 recovery specimen (LHV2429) under a top view perspective (Figure 6a). The upper boundary  
293 showed a relatively smoothed surface, consisting of fine Qz particles of  $\sim 1\text{--}2\ \mu\text{m}$  with sub-  
294 angular shape and submicron Gr flakes. It was consistent with Layer I identified in the thin  
295 section (Figure 6b). The enlarged image shows that the individual Qz particles were pasted on  
296 the surface by a large amount of small Gr flakes (Figure 6c). In contrast, the broken surface  
297 beneath the upper surface (see its position in Figure 6a) had relatively large particles ( $\sim 10\ \mu\text{m}$ )  
298 (Figure 6d). The individual Qz particles were mostly angular without visible foliation, while Gr  
299 appeared as isolated grains, suggesting relatively small deformation (Figure 6e). Note that  
300 numerous small particles were seen to be attached to the surfaces of Qz particles, but most were  
301 Qz debris (Figure 6f). All these features were similar to those observed in Layer III of specimens  
302 with intermediate Gr wt.% (i.e., 3 and 9 wt.%).

303

## 304 **4. Discussion**

### 305 **4.1 Mechanical and electrical behaviors of graphite-bearing faults**

#### 306 **4.1.1 Steady-state friction and conductivity relations of varying $X_{\text{Gr}}$ specimens**

307 To facilitate the comparison with previous works, the Gr fractions of all specimens were  
308 transformed from weight percentages to volume percentages ( $X_{\text{Gr}}$ ). Figure 7 shows  $\mu_{\text{ss}}$  and  $\sigma_{\text{ss}}$   
309 plotted against  $X_{\text{Gr}}$  for all specimens.

310 The  $\mu_{\text{ss}}\text{--}X_{\text{Gr}}$  data determined a threshold value ( $\sim 13.6\ \text{vol.}\%$ ), i.e., the  $X_{\text{Gr}}$  at which the  
311 frictional strength starts to decrease. A systematic increase of  $X_{\text{Gr}}$  from  $\sim 13.6$  to 30 vol.% led to a  
312 nonlinear  $\mu_{\text{ss}}$  decrease from 0.72 to 0.14. Thereafter, when  $X_{\text{Gr}}$  changed from 30 to 100 vol.%,  $\mu_{\text{ss}}$

313 gently approached  $\mu_{Gr}$  ( $\sim 0.1$ ). Oohashi et al. (2013) conducted frictional experiments on Gr–Qz  
 314 mixtures under similar conditions ( $\sigma_n = \sim 2$  MPa, dry,  $v_e = 0.2\text{--}56.0$  mm/s,  $X_{Gr} = 0\text{--}100$  vol.%)  
 315 and observed similar weakening trends as  $X_{Gr}$  increased (although they did not measure  $\sigma_{ss}$ ).  
 316 Following Oohashi et al. (2013), the relationship between  $\mu_{ss}\text{--}X_{Gr}$ , in this study, can be described  
 317 by

$$\mu_{ss}(X_{Gr}) = \frac{\mu_{Qz}\mu_{Gr}}{1+(X_{Gr}/X_{cw})^S} + \mu_{Gr}, \quad (2)$$

318 where  $\mu_{Qz}$  and  $\mu_{Gr}$  are the frictional coefficients of pure Qz and pure Gr, respectively. The  $\mu_{Qz}$   
 319 (0.73) was taken as the mean value of  $\mu_{ss}$  for the low- $X_{Gr}$  specimens ( $< 13.6$  vol.%), and  $\mu_{Gr}$  was  
 320 taken as 0.10 based on the  $\mu_{ss}$  values of pure Gr flakes.  $X_{cw}$  is the critical  $X_{Gr}$ , at which friction  
 321 reduces to the averages of  $\mu_{Qz}$  and  $\mu_{Gr}$ . The power exponent  $S$  indicates the slope of the  
 322 weakening with increasing  $X_{Gr}$ . The fitted parameters are presented in Table 3, and the  
 323 correlation coefficient ( $R^2$ ) is 0.94.

324 The  $\sigma_{ss}$  results show a significant sharp increase when  $X_{Gr}$  exceeds 3.4 vol.% (i.e., by more  
 325 than 7 orders of magnitude from 3.4 to 4.6 vol.%, Figure 7) and the  $\sigma_{ss}$  of pure Gr flakes ( $10^3$   
 326 S/m) is much greater than that of pure Qz particles ( $10^{-11}$  S/m). The enhancement of  $\sigma$  caused by  
 327 Gr has been observed in high pressure and/or high temperature experiments under static  
 328 conditions (Chen et al., 2017; Wang et al., 2013). In particular, Chen et al. (2017) explored the  
 329 electrical conductivity of similar Qz–Gr mixtures under non-sheared deformation and a wide  
 330 range of stress from 0.1 to 300.0 MPa. Following a previous study, percolation theory, i.e., a  
 331 model describing well the current transport properties through porous mediums (Stauffer &  
 332 Aharony, 2003), can explain the trend of the  $\sigma_{ss}\text{--}X_{Gr}$  curve via the following equation (Gueguen  
 333 & Dienes, 1989):

$$\sigma_{ss}(X_{Gr}) = \sigma_{Qz} + (\sigma_{Gr} - \sigma_{Qz}) \left[ \frac{\alpha(X_{Gr} - X_c)}{1 - \alpha X_c} \right]^r, \quad (X_{Gr} \geq 3.4\%) \quad (3)$$

334 where  $\sigma_{Qz}$  and  $\sigma_{Gr}$  are the electrical conductivities of the relatively insulated matrix (Qz) and  
 335 conductive inclusion (Gr),  $\alpha$  is the geometric factor of the conductor (Gr), and  $r$  is a  
 336 nondimensional parameter.  $X_c$  is the threshold value of  $X_{Gr}$ . It represents the critical volume  
 337 fraction of the conductor (Gr flakes in this study) for forming interconnected networks in the  
 338 specimens and depends on the geometry of the Gr flakes (Stauffer & Aharony, 2003). We note  
 339 that this study focuses on the effect of shear, especially the experimental data of low to

340 intermediate  $X_{Gr}$  specimens (< 20 vol.%). Therefore, data of high- $X_{Gr}$  specimens (> 20 vol.%) are  
 341 more scarce and cannot provide a better fitting for the power law growth. The fitted parameters  
 342 of Equation 3 are presented in Table 4, and the correlation coefficient ( $R^2$ ) is 0.98. Other fitting  
 343 details of the  $\mu_{ss}$ - $X_{Gr}$  and  $\sigma_{ss}$ - $X_{Gr}$  relationships can be found in Text S2.

344

#### 345 4.1.2 Representative microstructure interpretation

346 The critical  $X_{Gr}$  value for a  $\mu_{ss}$  decrease (~13.6 vol.%) was greater than that for a  $\sigma_{ss}$  increase  
 347 (3.4 vol.%) (as shown by the comparison between the  $\mu_{ss}$ - $X_{Gr}$  and  $\sigma_{ss}$ - $X_{Gr}$  curves in Figure 7). It  
 348 may be caused by the specific microstructural variations of the Qz-Gr mixtures. Consequently,  
 349 we divided this system into three regimes bounded by 3.4 and ~13.6 vol.%  $X_{Gr}$ , respectively. For  
 350 carbon-bearing rocks, the efficient electrical conductivity enhancement is mainly derived from  
 351 the microstructure of interconnected grain-boundary CMs (Duba & Shankland, 1982; Frost et al.,  
 352 1989; Mareschal et al., 1992). Associated with the SEM images in Figures 5 and 6, we propose  
 353 four classes of microstructures dependent on  $X_{Gr}$  (T1–T4, see the schematic diagrams beneath the  
 354 coordinate system of Figure 7) as follows:

355 (a) Pure Qz gouge ( $X_{Gr} = 0$ ). It exhibited insulating ( $\sim 10^{-11}$  S/m) and high-shear strength  
 356 properties ( $\mu_{ss} \approx 0.73$ ). A fault slip formed at the contact between Qz particles, and R-shear  
 357 surfaces developed throughout the entire mixture.

358 (b) Low  $X_{Gr}$  regime ( $0\% < X_{Gr} \leq 3.4\%$ ). Similar to pure Qz gouge, it presented low electrical  
 359 conduction ( $\sim 10^{-10}$  S/m) and high-level frictional strength (0.79–0.85). Three layers with  
 360 different Qz grain sizes (Layers I–III) developed, and similar results have been reported in  
 361 natural gouges (Hou et al., 2012; Wang et al., 2014). The non-foliated layer (Layer III), in the  
 362 bottom, comprised isolated angular Qz particles mixed with Gr flakes. The upper ~400  $\mu\text{m}$  SLZ  
 363 consisted of an ~200  $\mu\text{m}$  Layer I, and an ~200  $\mu\text{m}$  Layer II was produced near the side of the  
 364 specimen–cylinder boundary (grey layers in Figure 7). Moreover, low  $\sigma_{ss}$  of the mixtures in this  
 365 regime suggests the conductive Gr flakes cannot interconnect in this microstructure.

366 (c) Intermediate  $X_{Gr}$  regime ( $3.4\% < X_{Gr} \leq 13.6\%$ ). It was characterized by  $\sigma_{ss}$  enhancement  
 367 with increasing  $X_{Gr}$  ( $10^{-3}$  S/m  $< \sigma_{ss} < 4$  S/m). It also presented a three-layered microstructure  
 368 (Layers I–III) that differed from that of the low  $X_{Gr}$  regime. The Gr flakes were more frequent in

369 the pore spaces supported by the Qz framework with increasing  $X_{Gr}$ . Unimpregnated  
 370 microstructures of the slip surfaces in this regime showed a large number of tiny Gr flakes (~10  
 371 nm) pasted on the surface of Qz particles (Figures 6b and 6c). Thus, we propose that the SLZ of  
 372 Qz–Gr mixtures developed the fabric of graphite–cortex clasts (GCCs), i.e., comminuted  
 373 subangular Qz clasts ( $< 1 \mu\text{m}$ ) were surrounded by a cortex of concentric Gr layers (~10 nm),  
 374 which were composed of ultrafine pulverized Gr flakes (see the schematic cartoon extended from  
 375 the T3 texture). In contrast, Gr flakes in this regime could not be enriched to form lubricated slip  
 376 surfaces due to limited Gr fraction, and, therefore, the friction remained high ( $\mu_{ss} = 0.54\text{--}0.84$ ).  
 377 Moreover, GCCs may also exist in the low  $X_{Gr}$  regime, but due to the low  $X_{Gr}$ , they may not be  
 378 electrically connected.

379 (d) High  $X_{Gr}$  regime ( $13.6\% \lesssim X_{Gr} < 100\%$ ). It exhibited high  $\sigma_{ss}$  values ( $> 1 \text{ S/m}$ ) and low  
 380  $\mu_{ss}$  values (mostly  $< 0.2$ ). In particular, specimens in this regime had an initially conductive  
 381 structure ( $D_{sch} < 0.2 \text{ mm}$ ). Frictional weakening occurred during the experiment, and the  
 382 required slip distances were uniform ( $D_{\mu_{ss}} = 0.2\text{--}0.3 \text{ m}$ , Figures 4g–4h). When the  $X_{Gr}$  was  
 383 enhanced, the frictional level approached a pure Gr powder ( $\mu \approx 0.1$ ). In this case, the specimen  
 384 usually presented a narrow boundary shear band (Figure 5d) instead of a dispersive shear zone  
 385 (*cf.* low  $X_{Gr}$  regimes). The single shear zone (or shining surface) with an ~20  $\mu\text{m}$  thickness was  
 386 similar to that of the abandoned shear surface (Qz clumps in Figure 5e).

387

#### 388 4.1.3 Mechanisms responsible for electrical conduction and slip weakening

389 As addressed earlier, the  $\sigma$  of pure quartz and Gr–Qz mixtures with  $X_{Gr} \leq 3.4\%$  decreased  
 390 with initial shear displacement by several orders of magnitude. We interpreted that the initial  
 391 current flow was mainly through the grain contacts of large grains that developed under initial  
 392 static compaction, and that the transient decrease of electrical conductivity was due to the  
 393 destruction of large contacting asperities by initiating slip. A similar process has been proposed  
 394 by Yamashita et al. (2014) to explain the changes in electrical conductivity of gabbro specimens  
 395 sheared at subseismic velocities.

396 For the Gr–Qz mixtures in the intermediate  $X_{Gr}$  regime ( $3.4\% < X_{Gr} \lesssim 13.6\%$ ),  $\sigma$  showed  
 397 unstable fluctuations and eventually increased by more than six orders of magnitude during

398 progressive slip from  $D_{\sigma_{ch}}$  to  $D_{\sigma_{ss}}$ . In the steady state, they exhibited highly frictional strength  
399 (after  $D_{\mu_{ss}}$ ) and electrical conduction (after  $D_{\sigma_{ss}}$ ). Meanwhile, the SEM images showed a three-  
400 layered microstructure. We interpret that the conductive pathways mainly occurred in Layer I in  
401 the form of GCC fabric for the following reasons:

402 Layer III was almost undeformed and resembled an original preslip zone of the mixture.  
403 The fractures in the Qz particles may result from the axial compaction derived from the normal  
404 stress on the specimen. During the progressive slip, the original Qz particles were comminuted to  
405 micron- and even submicron-sized clasts, while subsequently producing an  $\sim 200 \mu\text{m}$  intensively  
406 foliated layer (Layer I) and an  $\sim 200 \mu\text{m}$  weakly foliated layer (Layer II), respectively. Compared  
407 with Layer I, Layer II exhibited a relatively larger Qz clast size and weak strain localization lying  
408 on the transitional phase between Layers I and III. Therefore, from the bottom to the top of the  
409 bulk gouge, the shear strain gradually increased, and the original Qz particles experienced a  
410 series of processes. They were axial compression, fragmentation, attrition, comminution, shear-  
411 induced clumping, and finally, attracting the ground Gr flakes to generate the GCC fabric in the  
412 SLZ. Several Qz clumps consisting of aggregated ultrafine Qz clasts with a thickness of  $\sim 10 \mu\text{m}$   
413 were abandoned in Layer I. The pore-filled Gr flakes between the Qz particles also underwent  
414 microstructural evolution from disconnection to interconnection. The instability of  $\sigma$  from  $\sigma_{ch}$  to  
415  $\sigma_{ss}$  corresponds to this process of microstructural transformation.

416 Our proposed GCC fabric is an unusual spherical aggregate. To our knowledge, this  
417 microstructure has not been published in other studies, including those of unsheared Gr–Qz  
418 mixtures (Chen et al., 2017) and sheared Gr–Qz mixtures at various slip rates (Oohashi et al.,  
419 2013). Its overall appearance resembles those of clay–clast aggregate or clast–cortex aggregate  
420 (CCA) fabrics. They were reported in previous investigations of shallow-depth seismogenic  
421 faults in the field or in rotary-shear experiments in laboratory (Boullier et al., 2009; Han &  
422 Hirose, 2012; Kim et al., 2022; Rempe et al., 2014; Sawai et al., 2012; Ujiie & Tsutsumi, 2010).  
423 We hypothesize that the formation process of the high friction–conduction GCC fabric is similar  
424 to that of the CCA formation model proposed by Boutareaud et al. (2010), i.e., electrostatically  
425 charged Qz particles by fractoemission and triboelectric effect attract Gr flakes to the "negative"  
426 Qz surface (Huang, 2002; Yoshida et al., 1997). Moreover, our results demonstrated that the  
427 GCC fabric was developed in samples with relatively low Gr contacts and required a relatively

428 large shear displacement under room-dry conditions. These conditions are also similar to the  
429 CCA formation conditions suggested by Han & Hirose (2012); Kim et al. (2022); Rempe et al.  
430 (2014).

431 The Gr–Qz mixtures in the high  $X_{Gr}$  regime ( $13.6\% \lesssim X_{Gr} < 100\%$ ) showed high  $\sigma$  values  
432 before shear deformation ( $> 0.3$  S/m), suggesting that the Gr flakes were texturally  
433 interconnected upon initial compaction. With continued shear,  $\sigma$  further increased to even higher  
434 values ( $> 1$  S/m), which can be attributed to the formation of the shear band. As reflected by the  
435 microstructure, the reduced porosity of the SLZ caused an apparent enrichment of Gr flakes and  
436  $\sigma$  enhancement (Figure 5d). It was supported by the previous compaction experiments that  
437 elevating the static stress could cause reduced porosity and, thus, the increase in electrical  
438 conductivity (Chen et al., 2017). Meanwhile, specimens in this high  $X_{Gr}$  regime were expected to  
439 readily weaken when subjected to shear deformation (Oohashi et al., 2013). We infer this is  
440 because of the apparent enrichment of Gr flakes due to porosity reduction and the development  
441 of slip-lubricated surfaces (Figure 5d). Interestingly, the thicknesses of the slip surfaces (10–20  
442  $\mu\text{m}$ ) were comparable to that of the Qz clumps developed in the intermediate  $X_{Gr}$  samples (see  
443 Figure 5e vs. Figure 5d). As indicated earlier, the latter were abandoned microslip zones during  
444 progressive slip, reflecting the migration of localized deformation. We infer that the single slip  
445 surface seen in the high  $X_{Gr}$  regime derived from a microslip zone developed at the earlier stage  
446 of shearing, whose resistance to shear is expected to be lower than that of the bulk layer. In all,  
447 these results suggest a strong interplay between the mineralogy, structure, and mechanical  
448 behavior of a fault.

449 Finally, we have used the percolation model (Equation 2) to fit the relationship between  $\sigma_{ss}$ –  
450  $X_{Gr}$  of the Gr–Qz mixtures with  $> 3.4\%$   $X_{Gr}$ . The applications of the percolation theory  
451 concerning the electrical current transport properties assume that the conductor is randomly  
452 located in a stable and isotropic structure (Stauffer & Aharony, 2003). Although we applied the  
453 percolation model to describe the conductive transport properties of a sheared fault gouge, the  
454 corresponding microstructure is assumed to have reached a similar quasi-steady state, reflecting  
455 an average structure of millions of particles. Admittedly, the proposed conductive textures in the  
456 intermediate to high  $X_{Gr}$  regimes in Figure 7 are anisotropic. However, the theory model can well  
457 express the relationship between  $\sigma_{ss}$ – $X_{Gr}$  under shear deformation in this study. It suggests that

458 the percolation model could have a much wider application. Nevertheless, it still requires further  
459 adaption of the percolation model to incorporate the anisotropic transport structure.

460 One possible development would involve the dimensions in which the conductive material  
461 (i.e., Gr) is distributed. Nominally, one could consider that the GCCs (graphite–cortex clasts)  
462 fabric is a two-dimensional (2D) structure, i.e., the Qz particles in the shear active zone are fully  
463 covered by Gr flakes (the schematic cartoon in Figure 7). However, as suggested by a simple  
464 calculation assuming Gr flakes of varied thicknesses (10–50 nm), obtaining such a structure  
465 requires a Gr content of at least 5.7 vol.%, higher than the threshold value of 3.4 vol.% obtained  
466 in the present experiments. At this point, an electrically conductive structure in one dimension  
467 (1D), i.e., the Gr flakes are attached end-to-end on the Qz surface to reach the electrodes, can  
468 help settle the discrepancy. The real GCC fabric in the samples might fall between 1D and 2D.  
469 Moreover, this does not conflict with the observation that much higher Gr contents (>13.6 vol%)  
470 are required to cause significant frictional weakening at otherwise the same conditions (Figure 7).  
471 This is because the frictional resistance of a shearing gouge is collectively determined by all the  
472 grain contacts within the active shear zone, such that the weakening would be more favorable  
473 when the Gr flakes somehow form a 2-D structure, requiring a higher Gr content. Nonetheless, at  
474 present, it is difficult to justify the aforementioned models. A combination of numerical  
475 simulations based on more sophisticated microstructure characteristics and updated percolation  
476 models is warranted in the future.

477

#### 478 4.1.4 Implications for high conductivity anomalies

479 The high conductivity anomalies in the fault zones observed by MT surveys are generally  
480 limited within the range of 0.100–0.005 S/m (e.g., Pous et al., 2004; Ritter et al., 2005;  
481 Wannamaker et al., 2002; Zhao et al., 2012). As illustrated in Figure 8, our data suggest that the  
482 Qz–Gr mixtures containing 5.4–8.1 vol.% Gr explain such observations (yellow stars in Figure  
483 8). However, this range is higher than those reported at fault zones by geological survey results  
484 (Manatschal, 1999; Ohashi et al., 2012).

485 Therefore, we subjected both the initial  $\sigma_0$  values and the fitted  $\sigma_{ss}-X_{Gr}$  curve of our study  
486 and those of previous experiments under higher static pressure conditions (Chen et al., 2017) for

487 further discussion. The  $\sigma_0$  values showed similar enhancement with increasing  $X_{Gr}$  to  $\sigma_{ss}$  values  
488 (from  $\sim 10^{-10}$  S/m to  $\sim 10^3$  S/m). Under static compaction, the higher the normal stress, the lower  
489 the threshold value ( $X_c$ , 6.0% under up to 300 MPa vs. 11.3% under 2 MPa), while the sheared  
490 specimen has the lowest  $X_c$  value (3.4%). Therefore, we posit two enhancement factors of  $X_c$   
491 (threshold value) and electrical conduction, i.e., shear deformation (a red shadow in Figure 8)  
492 and static compaction (a blue shadow in Figure 8). Meanwhile, deep Gr flakes can remain stable  
493 up to crustal depth (Selway, 2013). Therefore, assuming high pressure and temperature  
494 conditions, which are common in fault conditions, high  $\sigma$  values can be readily achieved in  
495 natural faults when  $X_{Gr}$  reaches 3.4%, given an extremely high growth rate across the critical  
496 value (upward pathway labeled by red dashed arrow in Figure 8).

497 The conductive properties of the upper crust can be affected by many electrical conduction  
498 factors, such as pressure, temperature, graphite (Frost et al., 1989; Nover et al., 1998), saline  
499 fluid (Guo & Keppler, 2019; Sinmyo & Keppler, 2017), sulfide (Watson et al., 2010), or partial  
500 melting (Chen et al., 2018). Furthermore, the coexistence of interconnected melt/fluids and Gr  
501 veins also seem to provide the best explanation in several low resistive fault zone derived from  
502 MT profiles (Wannamaker et al., 2002; Yu et al., 2020; Zhao et al., 2012) because the  
503 interconnected saline fluid improves the Gr-vein conduction (depositing hydrothermal Gr or  
504 promoting conductivity) (Kirilova et al., 2018b; Oohashi et al., 2012). To disentangle the effect  
505 of these mechanisms, we need to apply the control variable method, i.e., separately study these  
506 factors one by one to clarify their effects and finally summarize them and bring them together for  
507 comparison. Our work currently focuses only on the effect of Gr-bearing conductive networks on  
508 high conductivity anomalies at fault zones. Further experimental investigations at high  
509 temperatures and high pressure are necessary to constrain the mechanical and electrical  
510 conduction mechanisms of high conductivity brittle-to-ductile shear zones.

511

## 512 4.2 Electrical conductivity variations at initiation of frictional slip

### 513 4.2.1 Electrical conductivity jump as a potential indicator for fault slip

514 The results of our mechanical–electrical experiments at the millimeter scale show that the  $\sigma$ -  
515 jump phenomenon of Qz–Gr mixtures with  $> 4.6$  vol.% Gr ( $> 4$  wt.% Gr) occurred before

516 steady-state frictional slip, and even before the peak friction (see Figures 4a–4c vs. Figures 4d–4f,  
517 and the inset of Figure 9). This suggests that this jump can appear before steady-state fault slip,  
518 i.e., initiated frictional slip that may generate potential electromagnetic anomaly signals (the red  
519 area in Figure 9). In the following, we apply this phenomenon to natural Gr-enriched fault zones.

520 According to the classic earthquake nucleation theory, quasi-static or pre-slip occurs in the  
521 local area of a fault (i.e., the nucleation zone) before an earthquake (e.g., Dieterich, 1992; Rubin  
522 & Ampuero, 2005). With the expansion of the slip region, the fault appears to have irreversible  
523 dynamic expansion as it reaches the critical nucleation scale. Therefore, based on the above  
524 experimental observations, it is possible to detect an initiated slip of the fault by monitoring the  
525 change in the  $\sigma$  at the nucleation zone of the fault (see the abnormal electrical signals detected by  
526 the electrical resistivity stations in Figure 9). Besides the pre-slip, continuous or periodic creep  
527 (slow slip) of faults can also cause variations in electrical conductivity values. However, we  
528 cannot determine the cumulative slip displacement of the fault zone by electromagnetic data  
529 monitoring. If the slip has accumulated too large, that will lead to the development of a more  
530 mature shear zone structure (similar to the late stage in our experiment). The abrupt change in the  
531 electrical conductivity will hardly be observed. Therefore, thus far, for actual applications, our  
532 experimental results may not provide evidence for distinguishing fault creeps.

533

#### 534 4.2.2 Limitations and future development

535 Although this study is the first attempt to constrain the electrical response of carbon-bearing  
536 fault gouges under dynamic friction conditions, our conclusions have some limitations.

537 Firstly, the  $\sigma$  measurements used a single-frequency direct current method. However, the  
538 observed data of seismic georesistivity stations in the field cover a wide frequency range, which  
539 can reflect the electrical structure over various depth ranges (see the electrical current pathways  
540 at different depths in Figure 9). Although we sacrificed the accuracy of the electrical  
541 measurements, the transient electrical conductivity and the corresponding characteristic  
542 displacements of sheared fault gouge can be obtained in this study. In fact, our experimental data  
543 obtained based on the DC single-frequency method are close to those measured by the AC  
544 impedance spectroscopy on the same sheared Gr–Qz mixtures at the same conditions (Han et al.,  
545 2019). We believe that the precision of the experimental data meets the requirements of this study.

546 Secondly, only the specimens with > 17 vol.% Gr (or > 15 wt.% Gr) under our experimental  
547 conditions (i.e., low normal stress, room temperature, and dry conditions) exhibited the  $\sigma$ -jump  
548 phenomenon prior to the peak friction (Figure 4f). Fluid is widely present in nature fault zones  
549 and plays important roles in various aspects (Hickman et al., 1995). Previous studies also  
550 proposed that electrical anomalies in the brittle shallow fault zone are caused by pore fluid  
551 within rock fractures (Du, 2011; Park et al., 1993; Zhao & Qian, 1994). Against this background,  
552 the electromagnetic anomaly signals due to Gr interconnection revealed in this study may be  
553 limited to anhydrous fault environments, such as deep cataclasites with low porosities (bold blue  
554 dashed line across the preslip zone in Figure 9). Temperature and pressure conditions may also  
555 affect the results. Our previous experiments under static conditions revealed that elevated  
556 pressure can facilitate the grain-boundary Gr conduction and significantly reduce the threshold  
557 value (i.e., from 11.3 to 6.0 vol.% as pressure increases to 300 MPa, Figure 8). Taking this effect  
558 into account, the electromagnetic anomaly is expected to be generated under short shear  
559 displacement and/or lower threshold value. As indicated earlier, a natural Gr-bearing fault may  
560 have Gr content up to 12 wt.% (Manatschal, 1999; Oohashi et al., 2012). At elevated  
561 temperatures, plastic deformation mechanisms come to play an increasing role, and at some point,  
562 the silicate minerals begin to exhibit semiconductor behavior (e.g., >200–300 °C, Selway, 2013).  
563 All these processes can enhance the conductivity and affect the threshold values (Wang et al.,  
564 2013). To investigate these effects, systematical experiments using high-temperature and high-  
565 pressure deformation apparatuses such as the Paterson rig are planned in the future.

566

## 567 **5 Conclusions**

568 We designed a rotary-shear setup to monitor the transient electrical response of synthetic  
569 dry quartz (Qz)–graphite (Gr) mixtures in the shear-parallel direction during progressive slip.  
570 Long-displacement friction experiments (0.9–4.2 m) were performed at fixed normal stresses,  
571 slip rate, and N<sub>2</sub>-flushing atmosphere.

572 (1) Graphite volume fraction ( $X_{Gr}$ ) and slip displacement had important effects on the  
573 frictional coefficient ( $\mu$ ) and electrical conductivity ( $\sigma$ ) of the mixture. The steady-state frictional  
574 coefficient ( $\mu_{ss}$ ) of the mixtures with low  $X_G$  (< 13.6 vol.%) maintained high levels of frictional  
575 strength ( $\mu = 0.54$ – $0.80$ ), while the mixtures with high  $X_G$  (> 13.6 vol.%) showed remarkable slip

576 weakening behavior where the  $\mu_{ss}$  decreased with the increase of  $X_{Gr}$ . The  $\sigma$  of the mixtures with  
577  $\geq 4.6$  vol.%  $X_{Gr}$  abruptly increased ( $\sigma$  jump) with limited shear displacement; some  $\sigma$  jumps  
578 occurred even before the peak friction (as low as 0.2 mm). With continued shear, the steady-state  
579 electrical conductivity ( $\sigma_{ss}$ ) increased by more than seven orders of magnitude when  $X_{Gr} > 3.4$   
580 vol.%. The post-mortem microstructures revealed that the high  $\sigma_{ss}$  observed in the intermediate  
581 Gr content specimens (3.4–13.6 vol.%) was associated with an *ad-hoc* fabric (graphite-cortex  
582 clasts, GCCs) present in the principal slip zone. Excess Gr flakes can fill the pores and help  
583 develop Gr-coated mechanically lubricated surfaces.

584 (2) The percolation model can capture the relationship between the  $\sigma_{ss}$  and  $X_{Gr}$  of the Qz–Gr  
585 mixture. However, the percolation theory required adaption in the future to incorporate the  
586 anisotropic transport structure more accurately. Compared with the observations of  
587 magnetotelluric (MT) surveys, our experimental results revealed that dry sheared fault rocks  
588 containing 5.4–8.1 vol.% Gr may be responsible for the highly conductive anomalies at shear  
589 zones. Furthermore, considering the effect of high normal stress from our previous study (Chen  
590 et al., 2017), the high electrical conductivity ( $\sigma$ ) in the natural fault may also be achieved when  
591 the  $X_{Gr}$  is as low as 3.4 vol.%.

592 (3) The observed  $\sigma$ -jump phenomenon suggests that an initiated slip in the carbonaceous  
593 shear zone may generate potential electrical anomaly signals that can be detected by  
594 electromagnetic stations. The electrical anomaly due to Gr interconnection may be limited to  
595 anhydrous fault environments. Further experimental investigations for fluid-bearing specimens at  
596 high temperature and high pressure, applying the frequency sweep method, are required to  
597 constrain mechanical and electrical conduction mechanisms of shear zones.

598 **Acknowledgments**

599 This work was supported by the National Natural Science Foundation of China (Grants  
600 41904087) and the Basic Scientific Funding of Chinese National Nonprofit Institutes of the  
601 Institute of Geology, China Earthquake Administration (Grants IGCEA1821). We thank Yan  
602 Zhan and Xiangyu Sun for discussing explanations in MT surveys and Bo Zhao for analyzing  
603 grain size distribution. We also thank Prof. Y. Gueguen and an anonymous reviewer for their  
604 constructive comments, which greatly improved this manuscript.

605

606 **Open Research**

607 All the data used for this study have been made available through Mendeley Data  
608 (<https://doi.org/10.17632/p4bs2tb58h.1>) (Chen et al., 2023).

609

610 **Figure 1.** Illustration of the friction–conductivity testing system at the Institute of  
 611 Geology, China Earthquake Administration (IGCEA). (a) A low- to high-velocity  
 612 rotary shear apparatus, which provides a frictional environment. (b) Appearance of  
 613 the 4-wire (i.e., using wires 1–4) experimental assembly amplified from (a). The two  
 614 small figures in the upper right corner show a non-specimen assembly and a  
 615 specimen-bearing assembly before prepressing. (c) The electrical conductivity  
 616 measurement apparatus, i.e., Keithley low-level sensitive and specialty instruments.  
 617 They contain three models adapted to different electrical resistance ranges of Gr-  
 618 bearing specimens (the detailed settings are presented in Table 1). (d) Diagram of a  
 619 Gr-bearing specimen assembly adapted to transient electrical conductivity  
 620 measurement by the 2- or 4-wire setups. An arced arrow indicates the shear direction.  
 621  $P_n$  indicates constant normal stress. (e) A schematic representation of the specimen  
 622 and sections chosen for microstructural analysis (see Figure 5).

623

624 **Figure 2.** Frictional coefficient and electrical conductivity for the Gr–Qz mixtures  
 625 sheared at a normal stress of 2 MPa. (a–b) Frictional coefficient vs slip displacement.  
 626 (c–d) Electrical conductivity vs slip displacement. The slip displacement is plotted  
 627 on (panels a and c) logarithmic and (panels b and d) linear scales. The percentages in  
 628 the legend indicate the Gr contents of the specimens in weight ratio.  $D_{\sigma_{ch}}$ ,  $D_{\mu_{ss}}$ , and  
 629  $D_{\sigma_{ss}}$  denote the characteristic displacements at which the electrical conductivity  
 630 initiates significant changes and at which the evolution of friction coefficient and  
 631 electrical conductivity reach steady states, respectively (marked as yellow diamond,  
 632 pentagram, and square symbols on each curve, respectively). We note that the final  
 633 jump and hold-time data ( $v_e < 0.6$  mm/s) of all experimental values were removed.

634

635 **Figure 3.** Frictional coefficient and electrical conductivity for the Gr–Qz mixtures  
 636 sheared at a normal stress of 5 MPa. Details are the same as those in Figure 2.

637

638 **Figure 4.** Comparison of experimental data related to characteristic displacements.  
 639 (a–f) Electrical conductivity and friction coefficient plotted against displacement  
 640 data at displacements between  $D_{\sigma_{ch}}$  (diamond labels) and  $D_{\sigma_{ss}}$  (square labels) are  
 641 highlighted by bold solid lines. Gr fractions correspond to (panels a and d) 4–10  
 642 wt.%, (panels b and e) 9–12 wt.%, and (panels c and f) 15–50 wt.%. Further details  
 643 are the same as those in Figure 2.  $D_0$  denotes the characteristic displacements at  
 644 which the specimen initiates shear deformation (marked as a circle of the same color  
 645 on each curve). (g–h) Variations of  $D_{\sigma_{ch}}$ ,  $D_{\sigma_{ss}}$ , and  $D_{\mu_{ss}}$  vs Gr fraction in the Gr–Qz  
 646 mixtures sheared under normal stresses of 2 and 5 MPa. Definitions of the symbols  
 647 are the same as those in Figure 2.

648

649 **Figure 5.** BSE images of the Gr-bearing specimens sectioned parallel to the axis of  
 650 cylindrical host blocks. (a) 0 wt.% Gr, (b) and (e) 3 wt.% Gr, (c) and (f) 9 wt.% Gr,  
 651 and (d) 25 wt.% Gr, respectively. The specimen number, final slip displacement, Gr  
 652 content, and normal stress of each experiment are shown above the images. Yellow  
 653 dotted lines in panels b and c show boundaries of the three layers with different

654 degrees of shear deformation (Layers I to III with ascending shear deformation). Gr:  
655 graphite; Qz: Quartz; ER: Epoxy Resin.

656

657 **Figure 6.** Microphotographs of deformed and undeformed layers for specimen. It is  
658 an unepoxied piece of the gouge layer recovered after the run LHV2429 (12 wt.% Gr  
659 at 2 MPa). (a) Geometry of the specimen and location of the spot for SEM. (b–c) SE  
660 images of the upper surface of the slip-localized zone (akin to the top surface of  
661 Layer I in Figures 5b–5c). (d–f) BSE image of the weakly or undeformed zone (akin  
662 to Layer III in Figures 5b–5c).

663

664 **Figure 7.** Schematic diagram of the fitting  $\mu_{ss}$ – $X_{Gr}$  relationship (solid blue line), the  
665 fitted  $\sigma_{ss}$ – $X_{Gr}$  relationship (solid red line), and four classes of frictional textures for  
666 Gr–Qz mixtures. The cartoon shows the proposed graphite–cortex clast (GCC) fabric.

667

668 **Figure 8.** Electrical conductivity vs.  $X_{Gr}$ . Experimental values of the initial electrical  
669 conductivity ( $\sigma_0$ ) at 2 MPa (solid red line) and 5 MPa (solid blue line) and a fitting  
670 curve (solid black line) of the steady-state electrical conductivity ( $\sigma_{ss}$ ) plotted against  
671 the Gr volume percentage ( $X_{Gr}$ ) for the Qz–Gr mixtures. The grey dashed line shows  
672 the conductive trend of identical mixtures in this study under uniaxial compaction at  
673 0.1–300.0 MPa (Chen et al., 2017). The orange regime (0.100–0.005 S/m) indicates  
674 the general range of highly conductive field values in shear zones derived from  
675 magnetotelluric surveys (e.g., Pous et al., 2004; Ritter et al., 2005; Wannamaker et  
676 al., 2002; Zhao et al., 2012).

677

678 **Figure 9.** Schematic diagram of an electromagnetic station layout across a  
679 carbonaceous fault zone. The inset indicates the variations of shear stress ( $\tau$ ) and  
680 electrical conductivity ( $\sigma$ ) of the initiated slip zone.

681 **Table 1.** Summary of electrical conductivity measurement models.

Gr wt. %	$R_E$ range	Measurement model	Accuracy
0–3%	$> 200 \text{ G}\Omega$	4-wire setup (using wires 1–4), $R_E = E/I$ , where constant DC current ( $I$ ) is supplied by the 6221 AC and DC Current Source and electrical potential ( $E$ ) is measured by the 6514 System Electrometer.	$\pm 0.46\%$
4–12%	$200 \text{ }\Omega$ – $200 \text{ G}\Omega$	2-wire setup (using wires 1–2), where $R_E$ is directly measured by the 6514 System Electrometer.	$\pm 1.50\%$
15–100%	$< 200 \text{ }\Omega$	4-wire (using wires 1–4), $R_E = E/I$ , where $I$ is supplied by the 6221 AC and DC Current Source and $E$ is measured by the 2182A Nanovoltmeter.	$\pm 0.42\%$

682

**Table 2.** Summary of the obtained experimental data.

No.	Specimen	Gr%	error	$D_{\mu_{ss}}$	$\mu_{ss}$	$\mu_{ss}^{(+)(-)}$	$D_{\sigma_{ch}}$	$D_{\sigma_{ss}}$	$\sigma_0$	$\sigma_{ss}$	$\sigma_{ss}^{(+)}$	$\sigma_{ss}^{(-)}$
		vol.%	$\pm$ vol.%	m			m	m	S/m	S/m	S/m	S/m
<i>Series I (2 MPa)</i>												
LHV2051	100 wt.% Qz	0.00	0.00	nd	nd	nd	nd	0.894	$1.54 \times 10^{-7}$	$4.38 \times 10^{-11}$	$3.56 \times 10^{-11}$	$1.96 \times 10^{-11}$
LHV2416	3 wt.% Gr+97 wt.% Qz	3.44	0.08	2.229	0.79	0.01	nd	$2.89 \times 10^{-4}$	$1.10 \times 10^{-9}$	$8.68 \times 10^{-11}$	$9.39 \times 10^{-11}$	$4.51 \times 10^{-11}$
LHV1374	4 wt.% Gr+96 wt.% Qz	4.58	0.09	0.397	0.80	0.03	0.500	1.161	$1.80 \times 10^{-10}$	$1.40 \times 10^{-3}$	$1.16 \times 10^{-3}$	$6.34 \times 10^{-4}$
LHV1372	5 wt.% Gr+95 wt.% Qz	5.72	0.11	0.566	0.54	0.01	0.233	0.788	$5.53 \times 10^{-10}$	$5.90 \times 10^{-3}$	$5.05 \times 10^{-3}$	$2.72 \times 10^{-3}$
LHV1373	6 wt.% Gr+94 wt.% Qz	6.85	0.12	0.525	0.62	0.04	0.158	1.048	$3.59 \times 10^{-10}$	0.089	0.087	0.044
LHV1371	9 wt.% Gr+91 wt.% Qz	10.23	0.16	0.508	0.78	0.00	$7.01 \times 10^{-4}$	0.206	$6.93 \times 10^{-10}$	0.345	0.256	0.147
LHV2052	10 wt.% Gr+90 wt.% Qz	11.35	0.17	nd	nd	nd	0.004	0.113	$2.28 \times 10^{-10}$	0.018	$4.36 \times 10^{-3}$	$3.50 \times 10^{-3}$
LHV2429	12 wt.% Gr+88 wt.% Qz	13.57	0.20	nd	nd	nd	$1.94 \times 10^{-4}$	0.004	0.268	4.367	2.267	1.492
LHV1380/2050	15 wt.% Gr+85 wt.% Qz	16.89	0.23	0.321	0.62	0.03	$1.79 \times 10^{-4}$	0.009	1.679	1.473	0.060	0.058
LHV2418	25 wt.% Gr+75 wt.% Qz	27.74	0.31	0.150	0.19	0.01	$3.89 \times 10^{-4}$	0.003	32.59	54.61	9.211	7.882
LHV2419	50 wt.% Gr+50 wt.% Qz	53.53	0.37	0.339	0.11	0.00	$4.39 \times 10^{-4}$	0.003	171.0	421.5	31.68	29.47
<i>Series II (5 MPa)</i>												
LHV2057	100 wt.% Qz	0.00	0.00	nd	nd	nd	nd	0.170	$8.15 \times 10^{-8}$	$1.78 \times 10^{-11}$	$1.13 \times 10^{-12}$	$1.06 \times 10^{-12}$
LHV1823/2054	3 wt.% Gr+97 wt.% Qz	3.44	0.08	0.361	0.85	0.03	nd	0.594	$2.70 \times 10^{-10}$	$1.57 \times 10^{-10}$	$2.00 \times 10^{-11}$	$1.77 \times 10^{-11}$
LHV1375*	6 wt.% Gr+94 wt.% Qz	6.85	0.12	0.413	0.80	0.06	0.175	0.743	$8.65 \times 10^{-9}$	0.011	0.023	$7.29 \times 10^{-3}$
LHV2055	9 wt.% Gr+91 wt.% Qz	10.23	0.16	0.407	0.84	0.12	$7.94 \times 10^{-4}$	0.057	$5.64 \times 10^{-4}$	0.359	0.085	0.069
LHV2056	15 wt.% Gr+85 wt.% Qz	16.89	0.23	0.337	0.74	0.03	$5.98 \times 10^{-4}$	0.010	13.57	54.37	12.00	9.828
LHV2053	100 wt.% Gr	100	0.00	0.283	0.10	0.00	0.000	0.000	1095	1077	22.19	21.74

684 Gr: graphite; Qz: quartz;  $\mu_{ss}$ : steady-state frictional coefficient;  $\mu_{ss}^{(+)(-)}$ : standard deviation of  $\mu_{ss}$ ;  $D_{\mu_{ss}}$ : slip displacement as  $\mu$  achieved  $\mu_{ss}$ ;  $\sigma_0$ : initial electrical conductivity;  $\sigma_{ss}$ : steady-state  
685 electrical conductivity;  $\sigma_{ss}^{(+)}/\sigma_{ss}^{(-)}$ : standard deviation of  $\sigma_{ss}$ ;  $D_{\sigma_{ch}}$ : slip displacement as conductivity initiated logarithmic change;  $D_{\sigma_{ss}}$ : slip displacement as  $\sigma$  achieved  $\sigma_{ss}$ , and nd indicates that the  
686 parameter could not be determined due to erratic frictional behavior.

687 **Table 3.** Fitted parameters of Equation 2 for the relationships between  $\mu_{ss}$  and  $X_{Gr}$ . Fitted parameters proposed by  
 688 Oohashi et al. (2013) are also listed.

$\mu_{Qz}$	$\mu_{Gr}$	$X_{cw}$	$S$	Data source and slip rate
0.73	0.10	0.223	8.97	This study; 1 mm/s
0.65	0.09	0.128	1.82	Oohashi et al., 2013; 0.2 mm/s
0.57	0.09	0.118	1.56	Oohashi et al., 2013; 21–56 mm/s

689  $\mu_{Qz}$  and  $\mu_{Gr}$ :  $\mu$  of pure Qz and Gr, respectively;  $X_{cw}$ : critical slip-weakening fraction for  $X_{Gr}$ ;  $S$ : slope parameter.

690

691

692 **Table 4.** Fitted parameters of Equation 3 for the relationships between  $\sigma_{ss}$  and  $X_{Gr}$ . Fitted parameters proposed by  
 693 Chen et al. (2017) are also listed.

$X_c$ vol.%	$\sigma_{Qz}$ S/m	$\sigma_{Gr}$ S/m	$\alpha$	$r$	Data source and experiment conditions
11.3	$2.28 \times 10^{-10}$	>171.0			Initial compaction at 2 MPa
6.8	$2.70 \times 10^{-10}$	1095.0			Initial compaction at 5 MPa
3.4	$1.11 \times 10^{-10}$	1077.0	1.29	3.36	Post-shear at 2–5 MPa
6.0	$1.32 \times 10^{-10}$	889.6	3.37	2.53	Chen et al., 2017; uniaxial compression

694  $\alpha$ : geometric factor of the conductor (Gr);  $r$ : nondimensional parameter;  $X_c$ : threshold value of  $X_{Gr}$ ;  $\sigma_{Qz}$ : electrical

695 conductivity of the insulating matrix (Qz);  $\sigma_{Gr}$ : electrical conductivity of the conductor (Gr).

696

**References**

- 698       Boullier, A.-M., Yeh, E.-C., Boutareaud, S., Song, S.-R., & Tsai, C.-H. (2009). Microscale  
699 anatomy of the 1999 Chi-Chi earthquake fault zone. *Geochemistry, Geophysics, Geosystems*, *10*(3),  
700 Q03016. <https://doi.org/10.1029/2008GC002252>
- 701       Boulton, C., Yao, L., Faulkner, D. R., Townend, J., Toy, V. G., Sutherland, R., et al. (2017). High-  
702 velocity frictional properties of Alpine Fault rocks: Mechanical data, microstructural analysis, and  
703 implications for rupture propagation. *Journal of Structural Geology*, *97*, 71-92.  
704 <https://doi.org/10.1016/j.jsg.2017.02.003>
- 705       Boutareaud, S., Boullier, A.-M., Andréani, M., Calugaru, D.-G., Beck, P., Song, S.-R., et al. (2010).  
706 Clay clast aggregates in gouges: New textural evidence for seismic faulting. *Journal of Geophysical*  
707 *Research: Solid Earth*, *115*(B2), B02408. <https://doi.org/10.1029/2008JB006254>
- 708       Byerlee, J. (1978). Friction of rocks. *pure and applied geophysics*, *116*(4), 615-626.  
709 <https://doi.org/10.1007/bf00876528>
- 710       Chen, J.-Y., Yang, X.-S., & Chen, J.-Y. (2017). Experimental studies on the relationship between  
711 carbonaceous structure and electrical conductivity of the Longmenshan fault zone. *Chinese Journal of*  
712 *Geophysics (in Chinese)*, *60*(9), 3475-3492. <https://doi.org/10.6038/cjg20170917>
- 713       Chen, J. (2022). The Effect of Quartz Particle Size on the Frictional and Electrically Conductive  
714 Properties of Mixed Graphite–Quartz Gouges. *Frontiers in Earth Science*, *10*, 913315.  
715 <https://doi.org/10.3389/feart.2022.913315>
- 716       Chen, J., Chen, J., Yao, L., & Ma, X. (2023). Analytical data and mechanical-electrical data of  
717 synthetic Qz-Gr mixtures (Version 1) [Dataset]. Mendeley Data. <https://doi.org/10.17632/p4bs2tb58h.1>
- 718       Chen, J., Gaillard, F., Villaros, A., Yang, X., Laumonier, M., Jolivet, L., et al. (2018). Melting  
719 conditions in the modern Tibetan crust since the Miocene. *Nature communications*, *9*(1), 3515.  
720 <https://doi.org/10.1038/s41467-018-05934-7>
- 721       Chen, J., Yang, X., Ma, S., Yang, T., & Niemeijer, A. (2016). Hydraulic properties of samples  
722 retrieved from the Wenchuan earthquake Fault Scientific Drilling Project Hole-1 (WFSD-1) and the  
723 surface rupture zone: Implications for coseismic slip weakening and fault healing. *Geochemistry,*  
724 *Geophysics, Geosystems*, *17*(7), 2717-2744. <https://doi.org/10.1002/2016GC006376>
- 725       Colletini, C., Niemeijer, A., Viti, C., & Marone, C. (2009). Fault zone fabric and fault weakness.  
726 *Nature*, *462*, 907. <https://doi.org/10.1038/nature08585>
- 727       Colletini, C., Tesei, T., Scuderi, M. M., Carpenter, B. M., & Viti, C. (2019). Beyond Byerlee  
728 friction, weak faults and implications for slip behavior. *Earth and Planetary Science Letters*, *519*, 245-  
729 263. <https://doi.org/10.1016/j.epsl.2019.05.011>
- 730       Crawford, B. R., Faulkner, D. R., & Rutter, E. H. (2008). Strength, porosity, and permeability  
731 development during hydrostatic and shear loading of synthetic quartz-clay fault gouge. *Journal of*  
732 *Geophysical Research: Solid Earth*, *113*, B03207. <https://doi.org/10.1029/2006JB004634>
- 733       Dieterich, J. H. (1992). Earthquake nucleation on faults with rate-and state-dependent strength.  
734 *Tectonophysics*, *211*(1), 115-134. [https://doi.org/https://doi.org/10.1016/0040-1951\(92\)90055-B](https://doi.org/https://doi.org/10.1016/0040-1951(92)90055-B)
- 735       Du, X. (2011). Two types of changes in apparent resistivity in earthquake prediction. *Science*  
736 *China Earth Sciences*, *54*(1), 145-156. <https://doi.org/10.1007/s11430-010-4031-y>
- 737       Duba, A. G., & Shankland, T. J. (1982). Free carbon & electrical conductivity in the Earth's mantle.  
738 *Geophysical Research Letters*, *9*(11), 1271-1274. <https://doi.org/10.1029/GL009i011p01271>
- 739       Frost, B. R., Fyfe, W. S., Tazaki, K., & Chan, T. (1989). Grain-boundary graphite in rocks and  
740 implications for high electrical conductivity in the lower crust. *Nature*, *340*(6229), 134-136.

741 <https://doi.org/10.1038/340134a0>

742 Glover, P. W. J., & Ádám, A. (2008). Correlation between crustal high conductivity zones and  
743 seismic activity and the role of carbon during shear deformation. *Journal of Geophysical Research:*  
744 *Solid Earth*, 113(B12), B12210. <https://doi.org/10.1029/2008JB005804>

745 Glover, P. W. J., & Vine, F. J. (1992). Electrical conductivity of carbon-bearing granulite at raised  
746 temperatures and pressures. *Nature*, 360(6406), 723-726. <https://doi.org/10.1038/360723a0>

747 Gueguen, Y., & Dienes, J. (1989). Transport properties of rocks from statistics and percolation.  
748 *Mathematical Geology*, 21(1), 1-13. <https://doi.org/10.1007/BF00897237>

749 Guo, H., & Kepler, H. (2019). Electrical Conductivity of NaCl-Bearing Aqueous Fluids to  
750 900 °C and 5 GPa. *Journal of Geophysical Research: Solid Earth*.  
751 <https://doi.org/doi:10.1029/2018JB016658>

752 Haak, V., Simpson, F., Bahr, K., Bigalke, J., Eisel, M., Harms, U., et al. (1997). KTB and the  
753 electrical conductivity of the crust. *Journal of Geophysical Research*, 102(B8), 18289-18306.  
754 <https://doi.org/10.1029/96JB03861>

755 Han, M., Yang, X., Yao, L., Chen, J., & Ma, S. (2019). A research on the conductivity  
756 characteristics of carbon-rich fault zones based on the middle-to high-velocity frictional experiments.  
757 *Chinese Journal of Geophysics (in Chinese)*, 63(3), 967-981. <https://doi.org/10.6038/cjg2019M0143>

758 Han, R., & Hirose, T. (2012). Clay–clast aggregates in fault gouge: An unequivocal indicator of  
759 seismic faulting at shallow depths? *Journal of Structural Geology*, 43, 92-99.  
760 <https://doi.org/10.1016/j.jsg.2012.07.008>

761 Hickman, S., Sibson, R., & Bruhn, R. (1995). Introduction to special section: Mechanical  
762 involvement of fluids in faulting. *Journal of Geophysical Research: Solid Earth (1978–2012)*, 100(B7),  
763 12831-12840. <https://doi.org/10.1029/95JB01121>

764 Hirono, T., Ujiie, K., Ishikawa, T., Mishima, T., Hamada, Y., Tanimizu, M., et al. (2009).  
765 Estimation of temperature rise in a shallow slip zone of the megasplay fault in the Nankai Trough.  
766 *Tectonophysics*, 478(3-4), 215-220. <https://doi.org/10.1016/j.tecto.2009.08.001>

767 Honkura, Y., Oshiman, N., Matsushima, M., Barış, Ş., Kemal Tunçer, M., Bülent Tank, S., et al.  
768 (2013). Rapid changes in the electrical state of the 1999 Izmit earthquake rupture zone. *Nature*  
769 *communications*, 4(1), 2116. <https://doi.org/10.1038/ncomms3116>

770 Hou, L., Ma, S., Shimamoto, T., Chen, J., Yao, L., Yang, X., et al. (2012). Internal structures and  
771 high-velocity frictional properties of a bedding-parallel carbonate fault at Xiaojiaqiao outcrop activated  
772 by the 2008 Wenchuan earthquake. *Earthquake Science*, 25(3), 197-217.  
773 <https://doi.org/10.1007/s11589-012-0846-2>

774 Hou, M., He, Y., Jang, B. G., Sun, S., Zhuang, Y., Deng, L., et al. (2021). Superionic iron oxide–  
775 hydroxide in Earth’s deep mantle. *Nature Geoscience*, 14(3), 174-178. <https://doi.org/10.1038/s41561-021-00696-2>

776

777 Huang, Q. (2002). One possible generation mechanism of co-seismic electric signals. *Proceedings*  
778 *of the Japan Academy, Series B*, 78(7), 173-178. <https://doi.org/10.2183/pjab.78.173>

779 Kedar, L., Bond, C. E., & Muirhead, D. (2020). Carbon ordering in an aseismic shear zone:  
780 Implications for Raman geothermometry and strain tracking. *Earth and Planetary Science Letters*, 549,  
781 116536. <https://doi.org/10.1016/j.epsl.2020.116536>

782 Kim, J. H., Ree, J.-H., Hirose, T., & Ohashi, K. (2022). Formation of clast-cortex aggregates in  
783 experimental fault gouges. *Tectonophysics*, 839, 229524. <https://doi.org/10.1016/j.tecto.2022.229524>

784 Kirilova, M., Toy, V., Rooney, J. S., Giorgetti, C., Gordon, K. C., Collettini, C., et al. (2018a).

785 Structural disorder of graphite and implications for graphite thermometry. *Solid Earth*, 9(1), 223-231.  
786 <https://doi.org/10.5194/se-9-223-2018>

787 Kirilova, M., Toy, V. G., Timms, N., Halfpenny, A., Menzies, C., Craw, D., et al. (2018b). Textural  
788 changes of graphitic carbon by tectonic and hydrothermal processes in an active plate boundary fault  
789 zone, Alpine Fault, New Zealand. *Geological Society, London, Special Publications*, 453(1), 205-223.  
790 <https://doi.org/10.1144/SP453.13>

791 Kouketsu, Y., Shimizu, I., Wang, Y., Yao, L., Ma, S., & Shimamoto, T. (2017). Raman spectra of  
792 carbonaceous materials in a fault zone in the Longmenshan thrust belt, China; comparisons with those  
793 of sedimentary and metamorphic rocks. *Tectonophysics*, 699, 129-145.  
794 <https://doi.org/10.1016/j.tecto.2017.01.015>

795 Kuo, L.-W., Sone, H., Luzin, V., Yeh, E.-C., Hsu, Y.-J., & Tan, E. (2022). Gouge fabrics reset by  
796 thermal pressurization record stress on faults after earthquakes. *Geology*, 50, 1033-1037.  
797 <https://doi.org/10.1130/g50217.1>

798 Kuo, L. W., Li, H. B., Smith, S. A. F., Di Toro, G., Suppe, J., Song, S. R., et al. (2014). Gouge  
799 graphitization and dynamic fault weakening during the 2008 Mw 7.9 Wenchuan earthquake. *Geology*,  
800 42(1), 47-50. <https://doi.org/10.1130/g34862.1>

801 Logan, J. M., Dengo, C. A., Higgs, N. G., & Wang, Z. Z. (1992), Chapter 2 Fabrics of  
802 Experimental Fault Zones: Their Development and Relationship to Mechanical Behavior. in  
803 *International Geophysics*, edited by B. Evans and T.-f. Wong, pp. 33-67, Academic Press,  
804 doi:10.1016/S0074-6142(08)62814-4

805 Lu, J., Xie, T., Li, M., Wang, Y., Ren, Y., Gao, S., et al. (2016). Monitoring shallow resistivity  
806 changes prior to the 12 May 2008 M 8.0 Wenchuan earthquake on the Longmen Shan tectonic zone,  
807 China. *Tectonophysics*, 675, 244-257. <https://doi.org/10.1016/j.tecto.2016.03.006>

808 Lyu, M., Cao, S., Neubauer, F., Li, J., & Cheng, X. (2020). Deformation fabrics and strain  
809 localization mechanisms in graphitic carbon-bearing rocks from the Ailaoshan-Red River strike-slip  
810 fault zone. *Journal of Structural Geology*, 140, 104150. <https://doi.org/10.1016/j.jsg.2020.104150>

811 Ma, S., Shimamoto, T., Yao, L., Togo, T., & Kitajima, H. (2014). A rotary-shear low to high-  
812 velocity friction apparatus in Beijing to study rock friction at plate to seismic slip rates. *Earthquake*  
813 *Science*, 27(5), 469-497. <https://doi.org/10.1007/s11589-014-0097-5>

814 Madden, T. R., LaTorraca, G. A., & Park, S. K. (1993). Electrical conductivity variations around  
815 the Palmdale Section of the San Andreas Fault Zone. *Journal of Geophysical Research*, 98(B1), 795-  
816 808. <https://doi.org/10.1029/92jb00568>

817 Manatschal, G. (1999). Fluid- and reaction-assisted low-angle normal faulting: evidence from rift-  
818 related brittle fault rocks in the Alps (Err Nappe, eastern Switzerland). *Journal of Structural Geology*,  
819 21(7), 777-793. [https://doi.org/10.1016/S0191-8141\(99\)00069-3](https://doi.org/10.1016/S0191-8141(99)00069-3)

820 Mareschal, M., Fyfe, W. S., Percival, J., & Chan, T. (1992). Grain-boundary graphite in  
821 Kapuskasing gneisses and implications for lower-crustal conductivity. *Nature*, 357, 674-676.  
822 <https://doi.org/10.1038/357674a0>

823 Mathez, E. A., Roberts, J. J., Duba, A. G., Kronenberg, A. K., & Karner, S. L. (2008). Carbon  
824 deposition during brittle rock deformation: Changes in electrical properties of fault zones and potential  
825 geoelectric phenomena during earthquakes. *Journal of Geophysical Research: Solid Earth*, 113(B12),  
826 B12201. <https://doi.org/10.1029/2008jb005798>

827 Monteiro Santos, F. A., Mateus, A., Almeida, E. P., Pous, J., & Mendes-Victor, L. s. A. (2002). Are  
828 some of the deep crustal conductive features found in SW Iberia caused by graphite? *Earth and*

829 *Planetary Science Letters*, 201(2), 353-367. [https://doi.org/10.1016/S0012-821X\(02\)00721-5](https://doi.org/10.1016/S0012-821X(02)00721-5)

830 Moore, D. E., & Lockner, D. A. (2004). Crystallographic controls on the frictional behavior of dry  
831 and water-saturated sheet structure minerals. *Journal of Geophysical Research: Solid Earth*, 109(B3),  
832 B03401. <https://doi.org/10.1029/2003JB002582>

833 Moore, D. E., & Lockner, D. A. (2011). Frictional strengths of talc - serpentine and talc - quartz  
834 mixtures. *Journal of Geophysical Research: Solid Earth*, 116, B01403.  
835 <https://doi.org/10.1029/2010JB007881>

836 Nakamura, Y., Oohashi, K., Toyoshima, T., Satish-Kumar, M., & Akai, J. (2015). Strain-induced  
837 amorphization of graphite in fault zones of the Hidaka metamorphic belt, Hokkaido, Japan. *Journal of*  
838 *Structural Geology*, 72, 142-161. <https://doi.org/10.1016/j.jsg.2014.10.012>

839 Nover, G., Heikamp, S., Meurer, H. J., & Freund, D. (1998). In-Situ Electrical Conductivity and  
840 Permeability of Mid-Crustal Rocks from the Ktb Drilling: Consequences for High Conductive Layers  
841 in the Earth Crust. *Surveys in Geophysics*, 19(1), 73-85. <https://doi.org/10.1023/A:1006592016176>

842 Nover, G., Stoll, J. B., & von der Gönna, J. (2005). Promotion of graphite formation by tectonic  
843 stress - a laboratory experiment. *Geophysical Journal International*, 160(3), 1059-1067.  
844 <https://doi.org/10.1111/j.1365-246X.2005.02395.x>

845 Oohashi, K., Hirose, T., Kobayashi, K., & Shimamoto, T. (2012). The occurrence of graphite-  
846 bearing fault rocks in the Atotsugawa fault system, Japan: Origins and implications for fault creep.  
847 *Journal of Structural Geology*, 38, 39-50. <https://doi.org/10.1016/j.jsg.2011.10.011>

848 Oohashi, K., Hirose, T., & Shimamoto, T. (2011). Shear-induced graphitization of carbonaceous  
849 materials during seismic fault motion: Experiments and possible implications for fault mechanics.  
850 *Journal of Structural Geology*, 33(6), 1122-1134. <https://doi.org/10.1016/j.jsg.2011.01.007>

851 Oohashi, K., Hirose, T., & Shimamoto, T. (2013). Graphite as a lubricating agent in fault zones:  
852 An insight from low- to high-velocity friction experiments on a mixed graphite-quartz gouge. *Journal*  
853 *of Geophysical Research: Solid Earth*, 118, 1-18. <https://doi.org/10.1002/jgrb.50175>

854 Park, S. K., Johnston, M. J. S., Madden, T. R., Morgan, F. D., & Morrison, H. F. (1993).  
855 Electromagnetic precursors to earthquakes in the Ulf band: A review of observations and mechanisms.  
856 *Reviews of Geophysics*, 31(2), 117-132. <https://doi.org/10.1029/93RG00820>

857 Pous, J., Muñoz, G., Heise, W., Melgarejo, J. C., & Quesada, C. (2004). Electromagnetic imaging  
858 of Variscan crustal structures in SW Iberia: the role of interconnected graphite. *Earth and Planetary*  
859 *Science Letters*, 217(3), 435-450. [https://doi.org/10.1016/S0012-821X\(03\)00612-5](https://doi.org/10.1016/S0012-821X(03)00612-5)

860 Puellas, P., Ábalos, B., & Fernández-Armas, S. (2014). Graphite and quartz petrofabrics:  
861 Examples from the Ediacaran black quartzites of the Ossa-Morena Zone (SW Iberia). *Tectonophysics*,  
862 615-616, 53-68. <https://doi.org/10.1016/j.tecto.2013.12.018>

863 Rawat, R., & Sharma, R. (2011). Features and characterization of graphite in Almora Crystallines  
864 and their implication for the graphite formation in Lesser Himalaya, India. *Journal of Asian Earth*  
865 *Sciences*, 42(1), 51-64. <https://doi.org/10.1016/j.jseaes.2011.03.015>

866 Rempe, M., Smith, S. A. F., Ferri, F., Mitchell, T. M., & Di Toro, G. (2014). Clast-cortex  
867 aggregates in experimental and natural calcite-bearing fault zones. *Journal of Structural Geology*, 68,  
868 142-157. <https://doi.org/10.1016/j.jsg.2014.09.007>

869 Ritter, O., Hoffmann-Rothe, A., Bedrosian, P. A., Weckmann, U., & Haak, V. (2005). Electrical  
870 conductivity images of active and fossil fault zones. *Geological Society, London, Special Publications*,  
871 245(1), 165-186. <https://doi.org/10.1144/gsl.sp.2005.245.01.08>

872 Roberts, J. J., Duba, A. G., Mathez, E. A., Shankland, T. J., & Kinzler, R. (1999). Carbon-

873 enhanced electrical conductivity during fracture of rocks. *Journal of Geophysical Research: Solid*  
874 *Earth*, 104(B1), 737-747. <https://doi.org/10.1029/1998jb900032>

875 Rubin, A. M., & Ampuero, J. P. (2005). Earthquake nucleation on (aging) rate and state faults.  
876 *Journal of Geophysical Research: Solid Earth*, 110(B11). <https://doi.org/10.1029/2005jb003686>

877 Rutter, E. H., Hackston, A. J., Yeatman, E., Brodie, K. H., Mecklenburgh, J., & May, S. E. (2013).  
878 Reduction of friction on geological faults by weak-phase smearing. *Journal of Structural Geology*, 51,  
879 52-60. <https://doi.org/10.1016/j.jsg.2013.03.008>

880 Sawai, M., Shimamoto, T., & Togo, T. (2012). Reduction in BET surface area of Nojima fault  
881 gouge with seismic slip and its implication for the fracture energy of earthquakes. *Journal of Structural*  
882 *Geology*, 38, 117-138. <https://doi.org/10.1016/j.jsg.2012.01.002>

883 Selway, K. (2013). On the causes of electrical conductivity anomalies in tectonically stable  
884 lithosphere. *Surveys in Geophysics*, 35(1), 219-257. <https://doi.org/10.1007/s10712-013-9235-1>

885 Sinmyo, R., & Keppler, H. (2017). Electrical conductivity of NaCl-bearing aqueous fluids to  
886 600 °C and 1 GPa. *Contributions to Mineralogy and Petrology*, 172(1), 4.  
887 <https://doi.org/10.1007/s00410-016-1323-z>

888 Stauffer, D., & Aharony, A. (2003). *Introduction to percolation theory*, London: Taylor & Francis,  
889 Takahashi, M., Mizoguchi, K., Kitamura, K., & Masuda, K. (2007). Effects of clay content on the  
890 frictional strength and fluid transport property of faults. *Journal of Geophysical Research: Solid Earth*,  
891 112(B8), B08206. <https://doi.org/10.1029/2006JB004678>

892 Tembe, S., Lockner, D. A., & Wong, T.-F. (2010). Effect of clay content and mineralogy on  
893 frictional sliding behavior of simulated gouges: Binary and ternary mixtures of quartz, illite, and  
894 montmorillonite. *Journal of Geophysical Research*, 115, B03416.  
895 <https://doi.org/10.1029/2009JB006383>

896 Togo, T., Shimamoto, T., Ma, S., Wen, X., & He, H. (2011). Internal structure of Longmenshan  
897 fault zone at Hongkou outcrop, Sichuan, China, that caused the 2008 Wenchuan earthquake.  
898 *Earthquake Science*, 24(3), 249-265. <https://doi.org/10.1007/s11589-011-0789-z>

899 Ujiie, K., & Tsutsumi, A. (2010). High-velocity frictional properties of clay-rich fault gouge in a  
900 megasplay fault zone, Nankai subduction zone. *Geophysical Research Letters*, 37(24), L24310.  
901 <https://doi.org/10.1029/2010gl046002>

902 Wang, D., Karato, S.-i., & Jiang, Z. (2013). An experimental study of the influence of graphite on  
903 the electrical conductivity of olivine aggregates. *Geophysical Research Letters*, 40(10), 2028-2032.  
904 <https://doi.org/10.1002/grl.50471>

905 Wang, Y., Ma, S., Shimamoto, T., Yao, L., Chen, J., Yang, X., et al. (2014). Internal structures and  
906 high-velocity frictional properties of Longmenshan fault zone at Shexigou activated during the 2008  
907 Wenchuan earthquake. *Earthquake Science*, 27(5), 499-528. [https://doi.org/10.1007/s11589-014-0096-](https://doi.org/10.1007/s11589-014-0096-6)  
908 [6](https://doi.org/10.1007/s11589-014-0096-6)

909 Wannamaker, P. E., Jiracek, G. R., Stodt, J. A., Caldwell, T. G., Gonzalez, V. M., McKnight, J. D.,  
910 et al. (2002). Fluid generation and pathways beneath an active compressional orogen, the New Zealand  
911 Southern Alps, inferred from magnetotelluric data. *Journal of Geophysical Research: Solid Earth*,  
912 107(B6), ETG 6-1-ETG 6-20. <https://doi.org/10.1029/2001JB000186>

913 Watson, H. C., Roberts, J. J., & Tyburczy, J. A. (2010). Effect of conductive impurities on  
914 electrical conductivity in polycrystalline olivine. *Geophysical Research Letters*, 37(2), L02302.  
915 <https://doi.org/10.1029/2009gl041566>

916 Yamashita, F., Fukuyama, E., & Mizoguchi, K. (2014). Probing the slip-weakening mechanism of

917 earthquakes with electrical conductivity: Rapid transition from asperity contact to gouge comminution.  
918 *Geophysical Research Letters*, 41(2), 341-347. <https://doi.org/10.1002/2013gl058671>

919 Yao, L., Ma, S., Shimamoto, T., & Togo, T. (2013a). Structures and high-velocity frictional  
920 properties of the Pingxi fault zone in the Longmenshan fault system, Sichuan, China, activated during  
921 the 2008 Wenchuan earthquake. *Tectonophysics*, 599, 135-156.  
922 <https://doi.org/10.1016/j.tecto.2013.04.011>

923 Yao, L., Shimamoto, T., Ma, S., Han, R., & Mizoguchi, K. (2013b). Rapid post-seismic strength  
924 recovery of Pingxi fault gouge from the Longmenshan fault system: Experiments and implications for  
925 the mechanisms of high-velocity weakening of faults. *Journal of Geophysical Research: Solid Earth*,  
926 118, 1-17. <https://doi.org/10.1002/jgrb.50308>

927 Yoshida, S., Uyeshima, M., & Nakatani, M. (1997). Electric potential changes associated with slip  
928 failure of granite: Preseismic and coseismic signals. *Journal of Geophysical Research: Solid Earth*,  
929 102(B7), 14883-14897. <https://doi.org/10.1029/97JB00729>

930 Yu, N., Unsworth, M., Wang, X., Li, D., Wang, E., Li, R., et al. (2020). New Insights Into Crustal  
931 and Mantle Flow Beneath the Red River Fault Zone and Adjacent Areas on the Southern Margin of the  
932 Tibetan Plateau Revealed by a 3-D Magnetotelluric Study. *Journal of Geophysical Research: Solid*  
933 *Earth*, 125(10), e2020JB019396. <https://doi.org/10.1029/2020jb019396>

934 Zhao, G., Unsworth, M. J., Zhan, Y., Wang, L., Chen, X., Jones, A. G., et al. (2012). Crustal  
935 structure and rheology of the Longmenshan and Wenchuan Mw 7.9 earthquake epicentral area from  
936 magnetotelluric data. *Geology*, 40(12), 1139-1142. <https://doi.org/10.1130/g33703.1>

937 Zhao, Y., & Qian, F. (1994). Geoelectric precursors to strong earthquakes in China.  
938 *Tectonophysics*, 233(1), 99-113. [https://doi.org/10.1016/0040-1951\(94\)90223-2](https://doi.org/10.1016/0040-1951(94)90223-2)

939 Zhuang, Y., Su, X., Salke, N. P., Cui, Z., Hu, Q., Zhang, D., et al. (2021). The effect of nitrogen on  
940 the compressibility and conductivity of iron at high pressure. *Geoscience Frontiers*, 12(2), 983-989.  
941 <https://doi.org/https://doi.org/10.1016/j.gsf.2020.04.012>

942 Zulauf, G., Palm, S., Petschick, R., & Spies, O. (1999). Element mobility and volumetric strain in  
943 brittle and brittle–viscous shear zones of the superdeep well KTB (Germany). *Chemical geology*,  
944 156(1-4), 135-149. [https://doi.org/10.1016/S0009-2541\(98\)00189-2](https://doi.org/10.1016/S0009-2541(98)00189-2)

945

**Figure 1.**

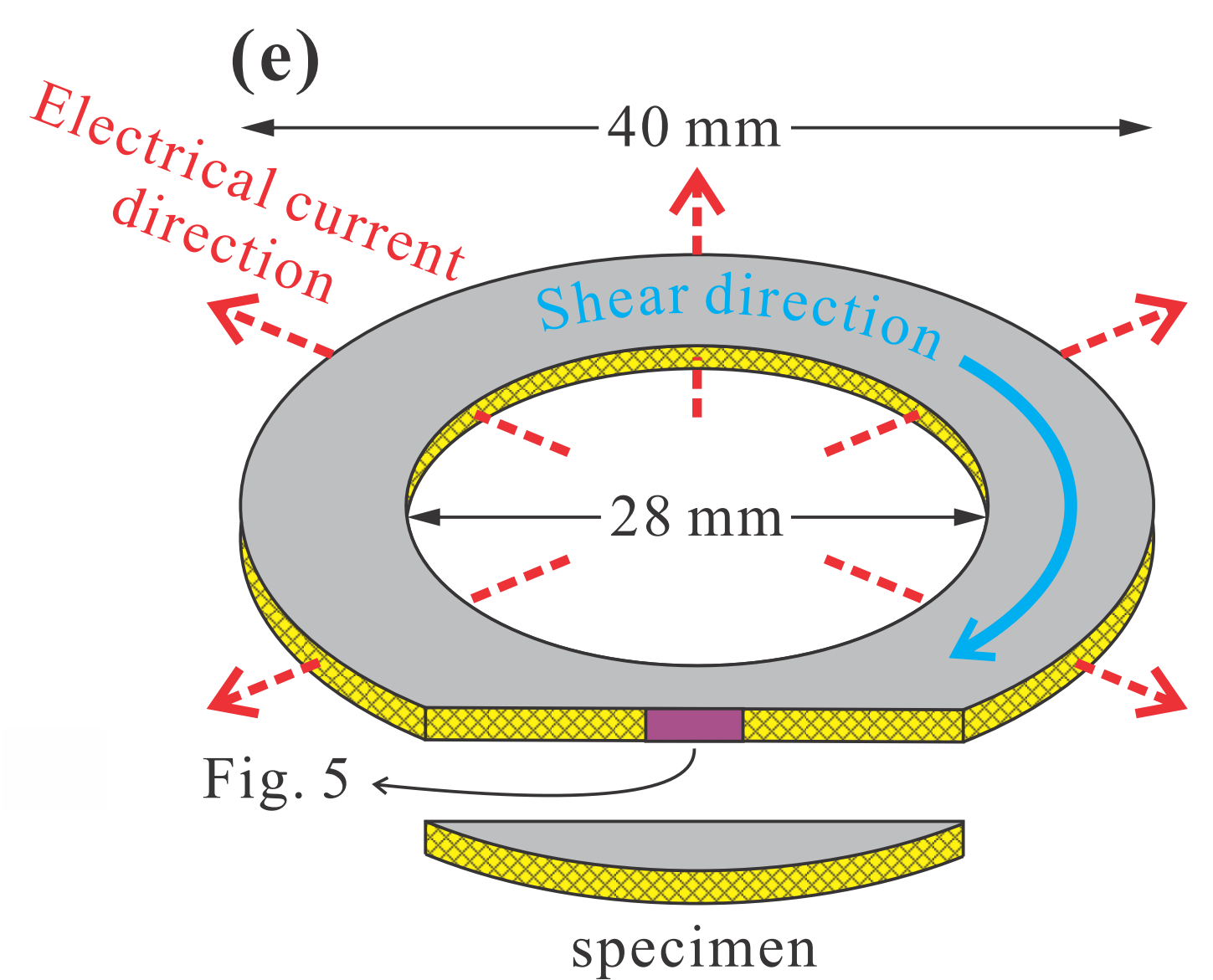
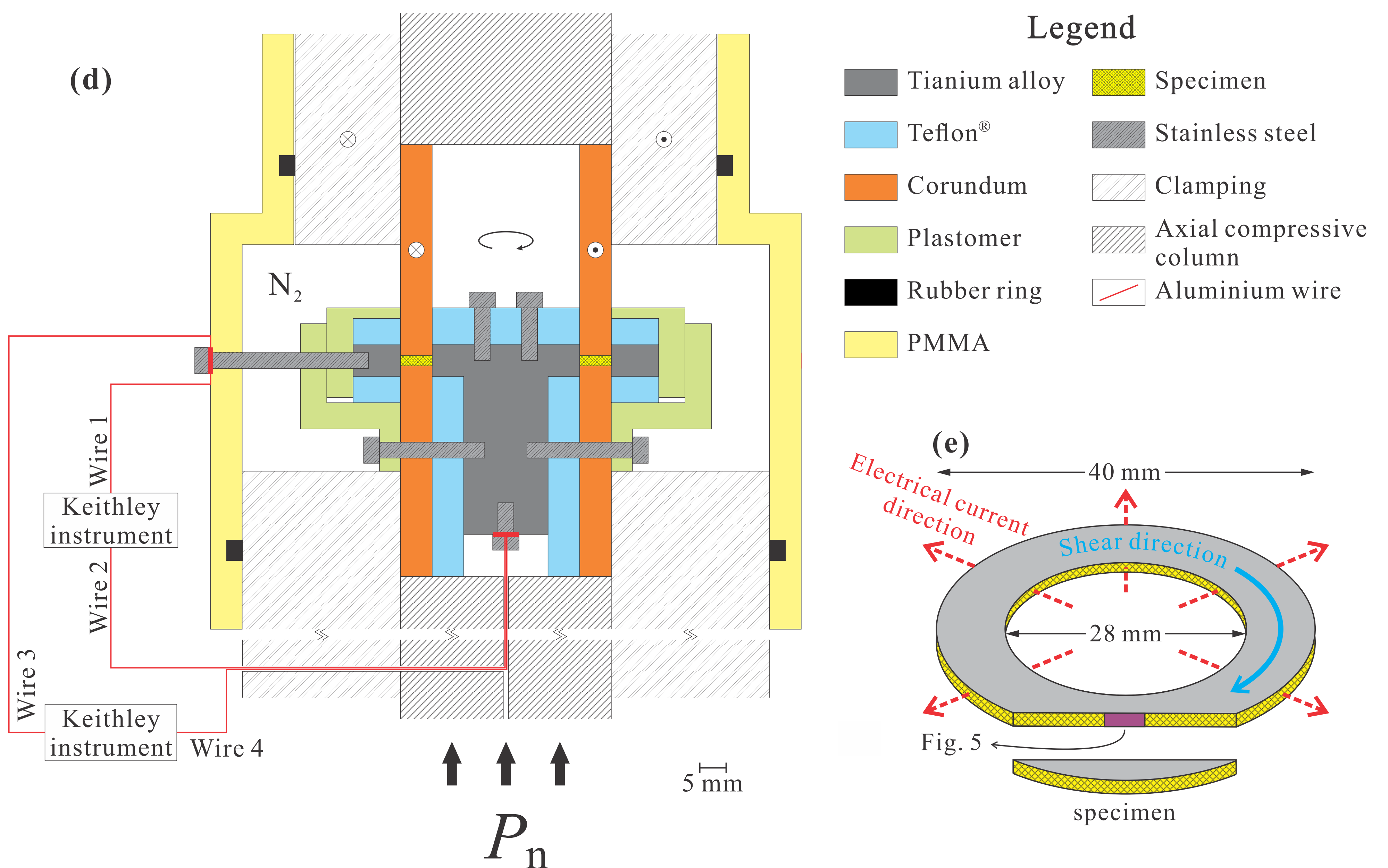
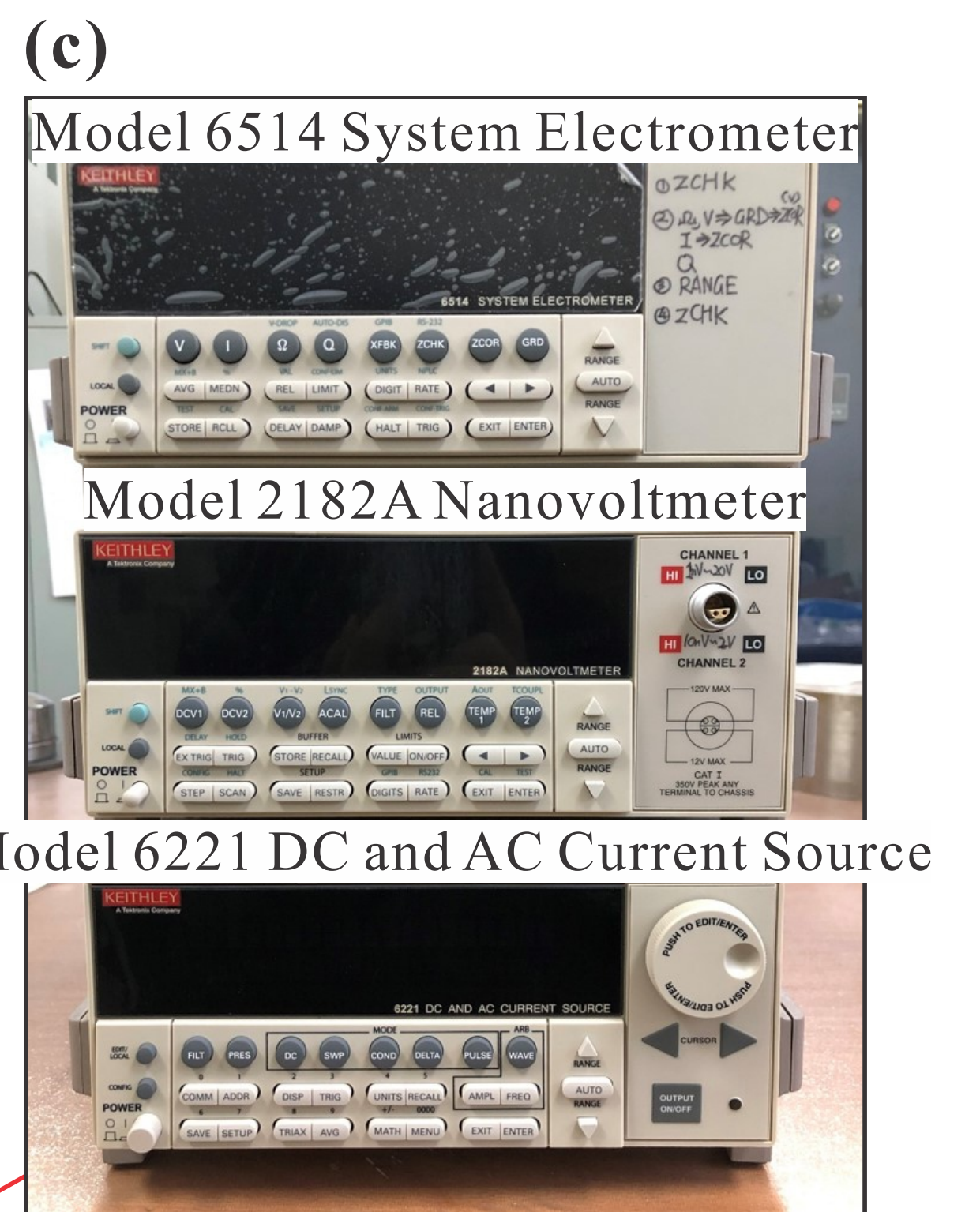
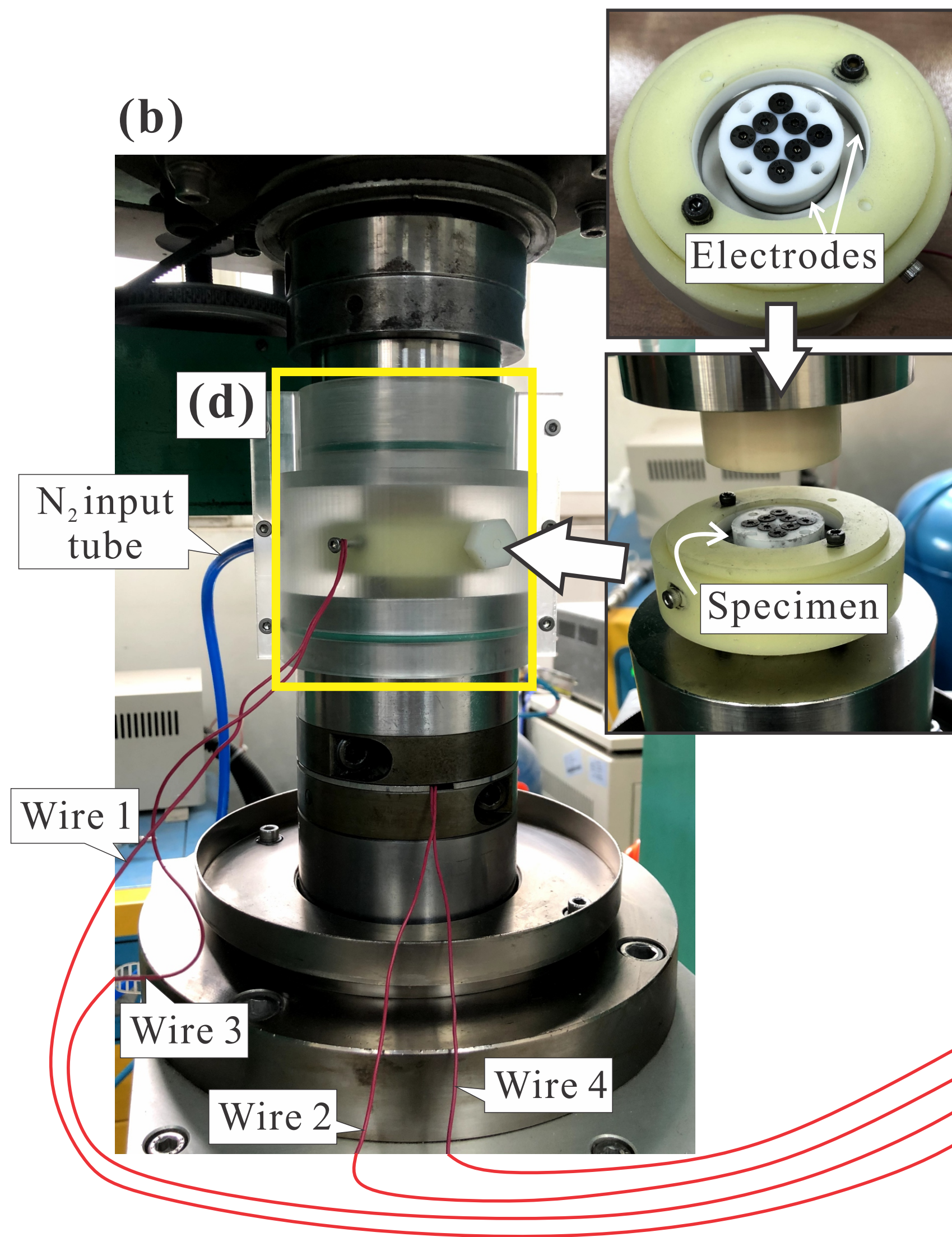
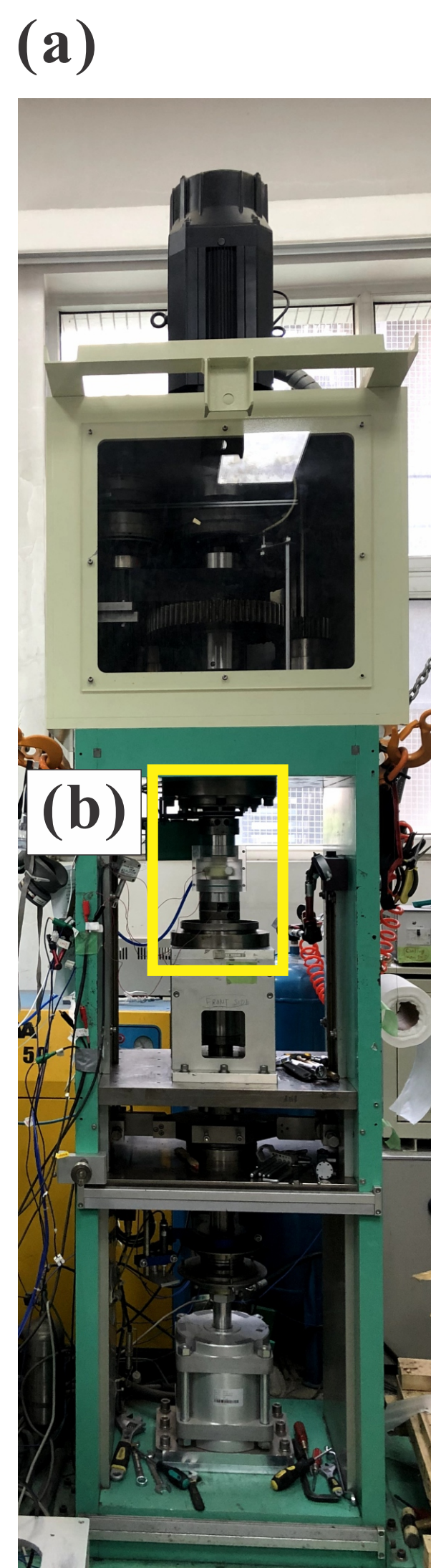


Figure 2.

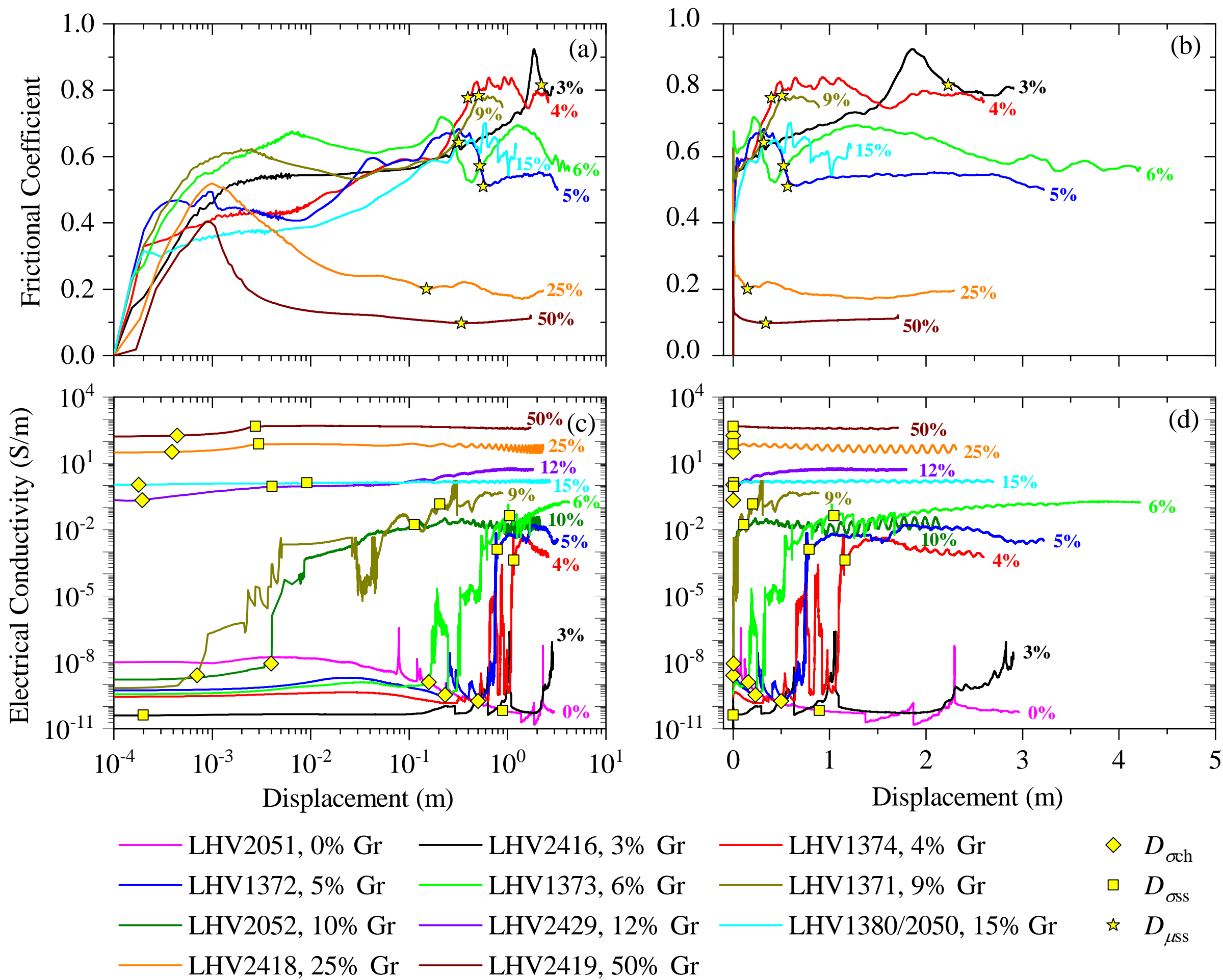


Figure 3.

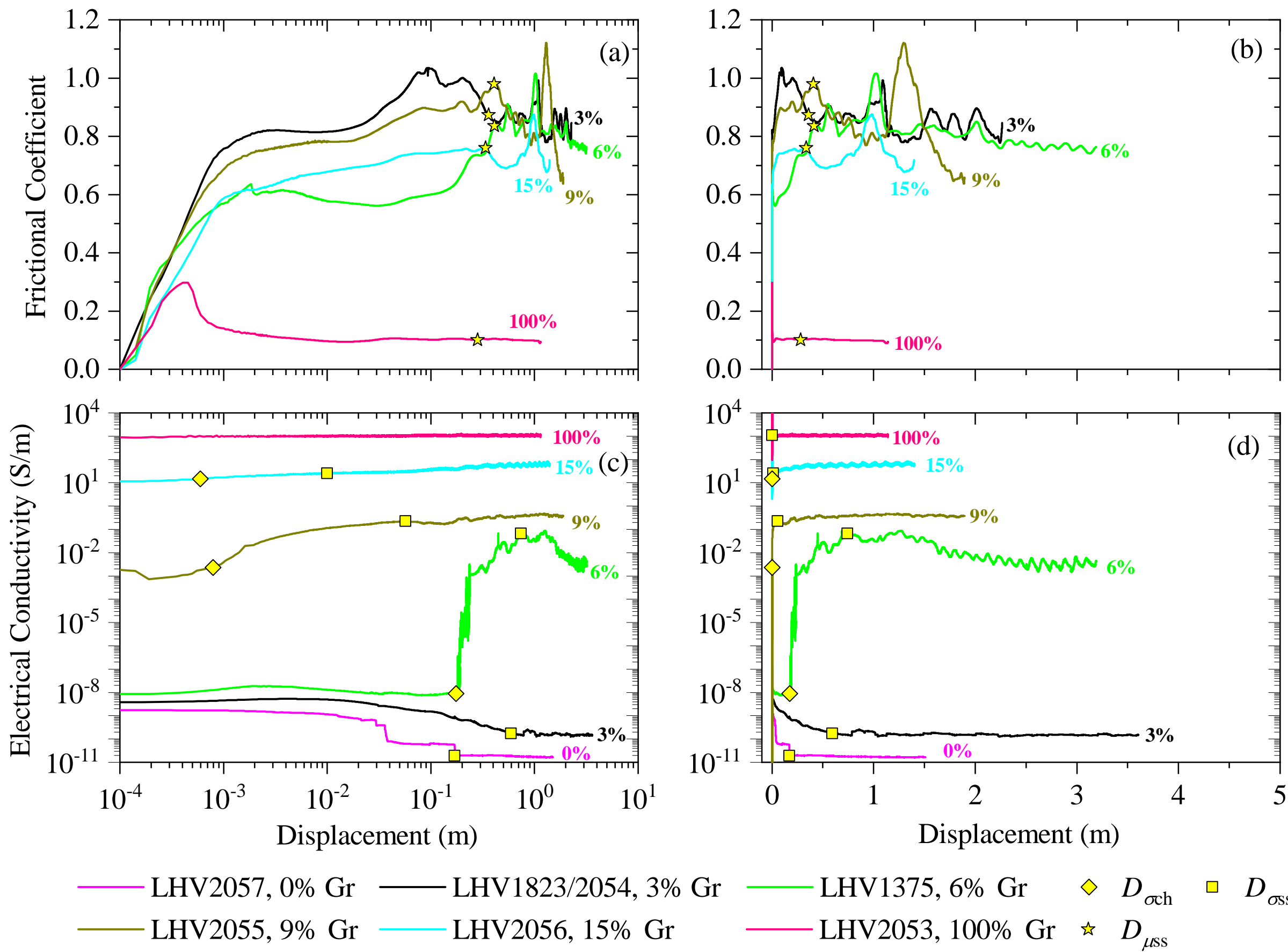


Figure 4.

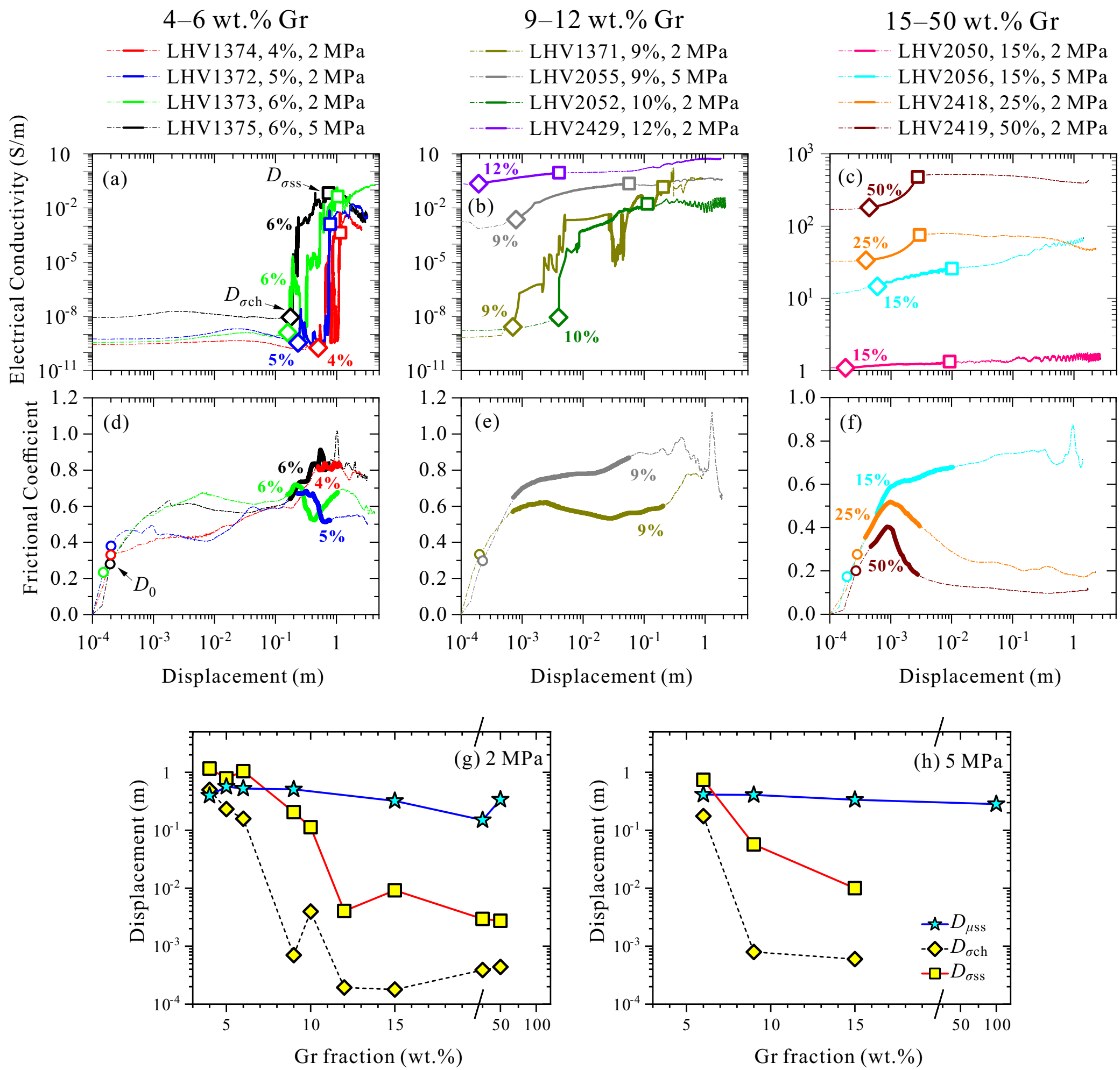


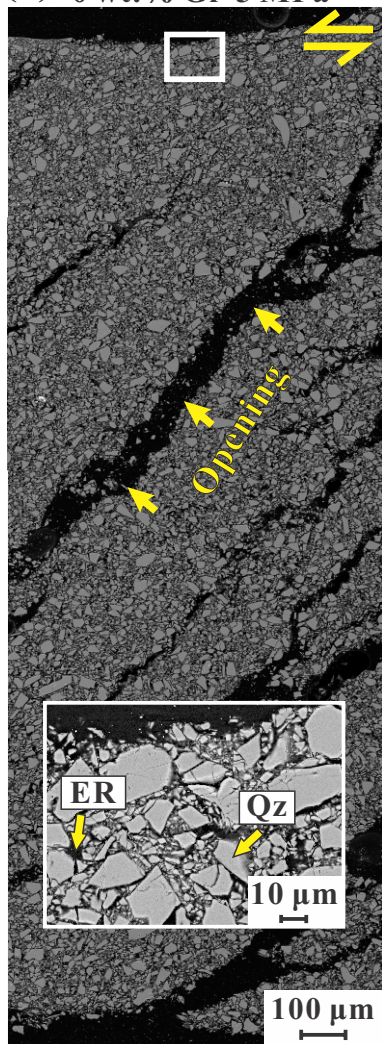
Figure 5.

LHV2055

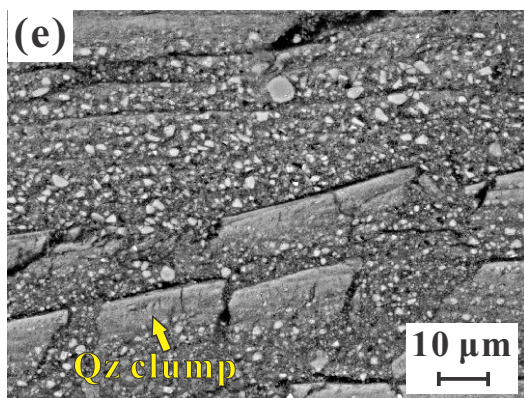
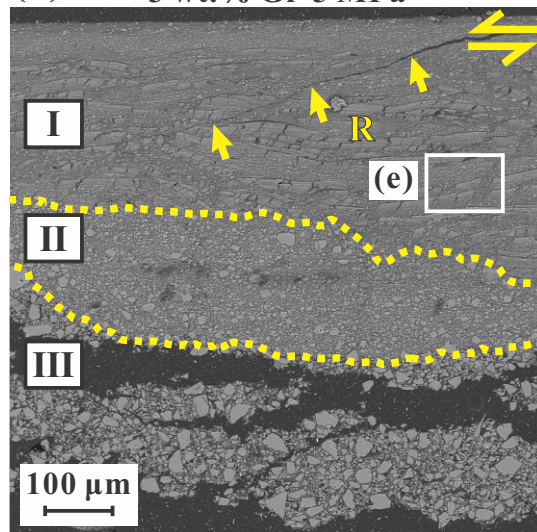
LHV2418



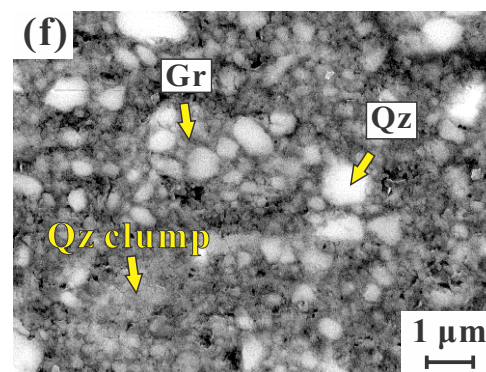
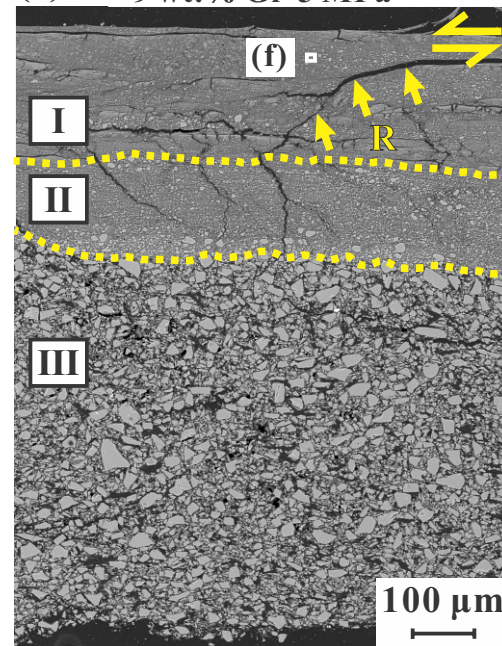
LHV2057 (1.55 m)  
(a) 0 wt.% Gr-5 MPa



LHV2054 (2.28 m)  
(b) 3 wt.% Gr-5 MPa



LHV2055 (1.90 m)  
(c) 9 wt.% Gr-5 MPa



LHV2418 (2.34 m)  
(d) 25 wt.% Gr-2 MPa

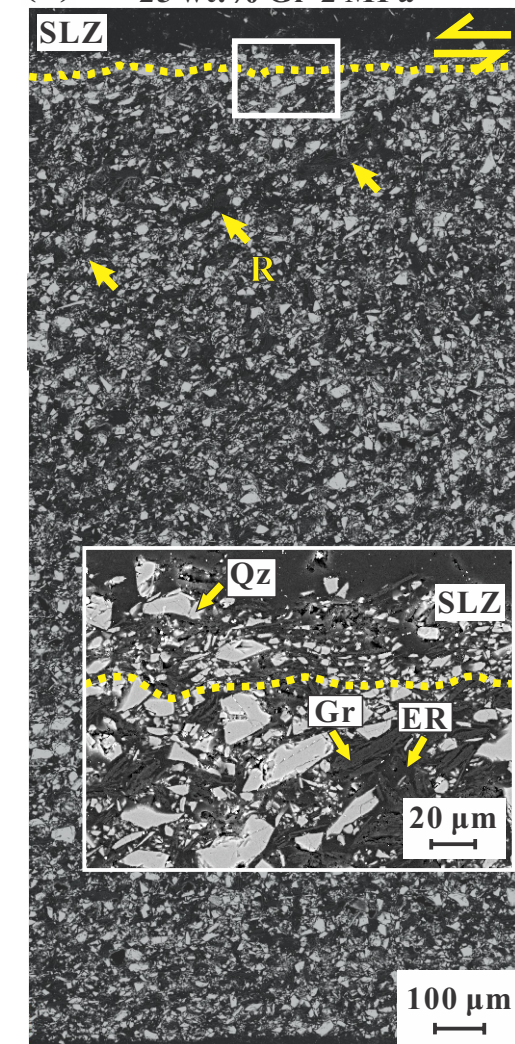
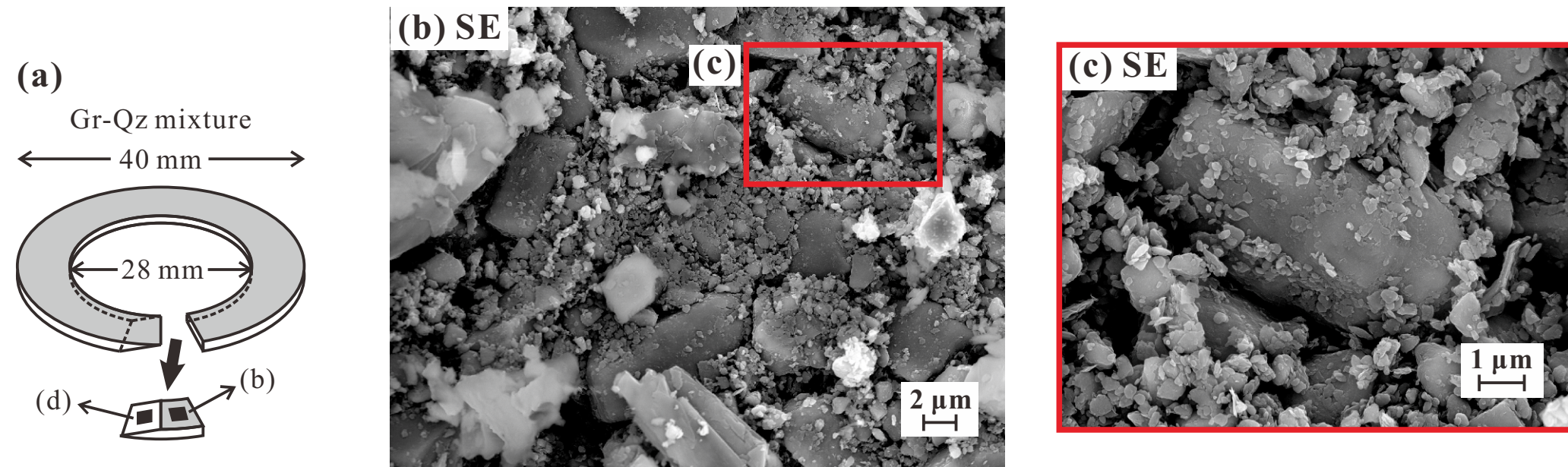


Figure 6.

# LHV2429 (1.84 m) 12 wt.% Gr-2 MPa

## Layer I *Intensive Foliation*



## Layer III *Non-Foliation*

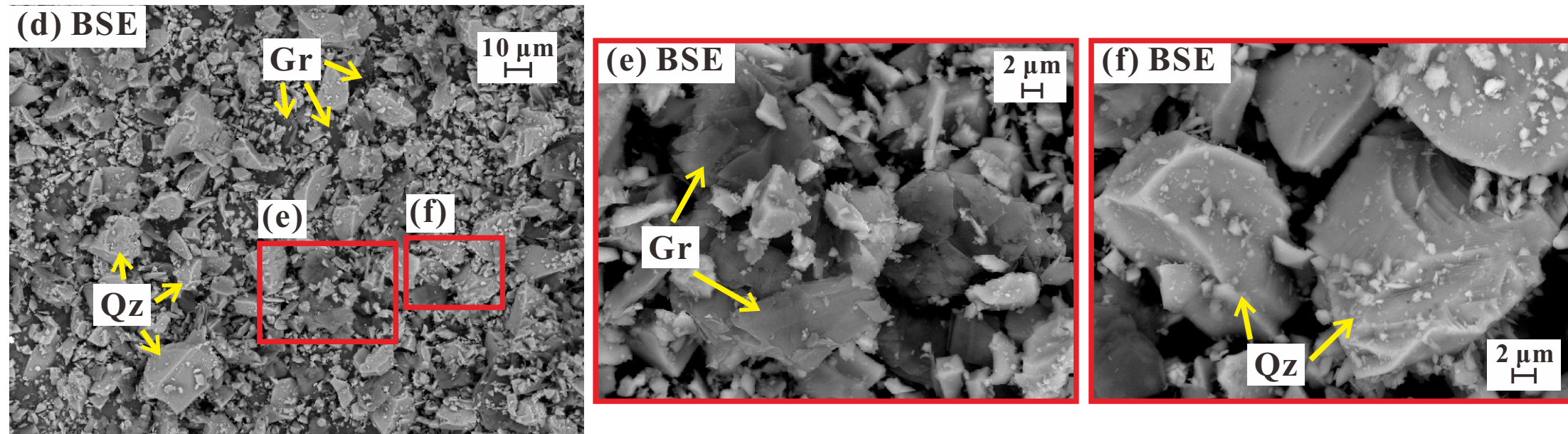


Figure 7.

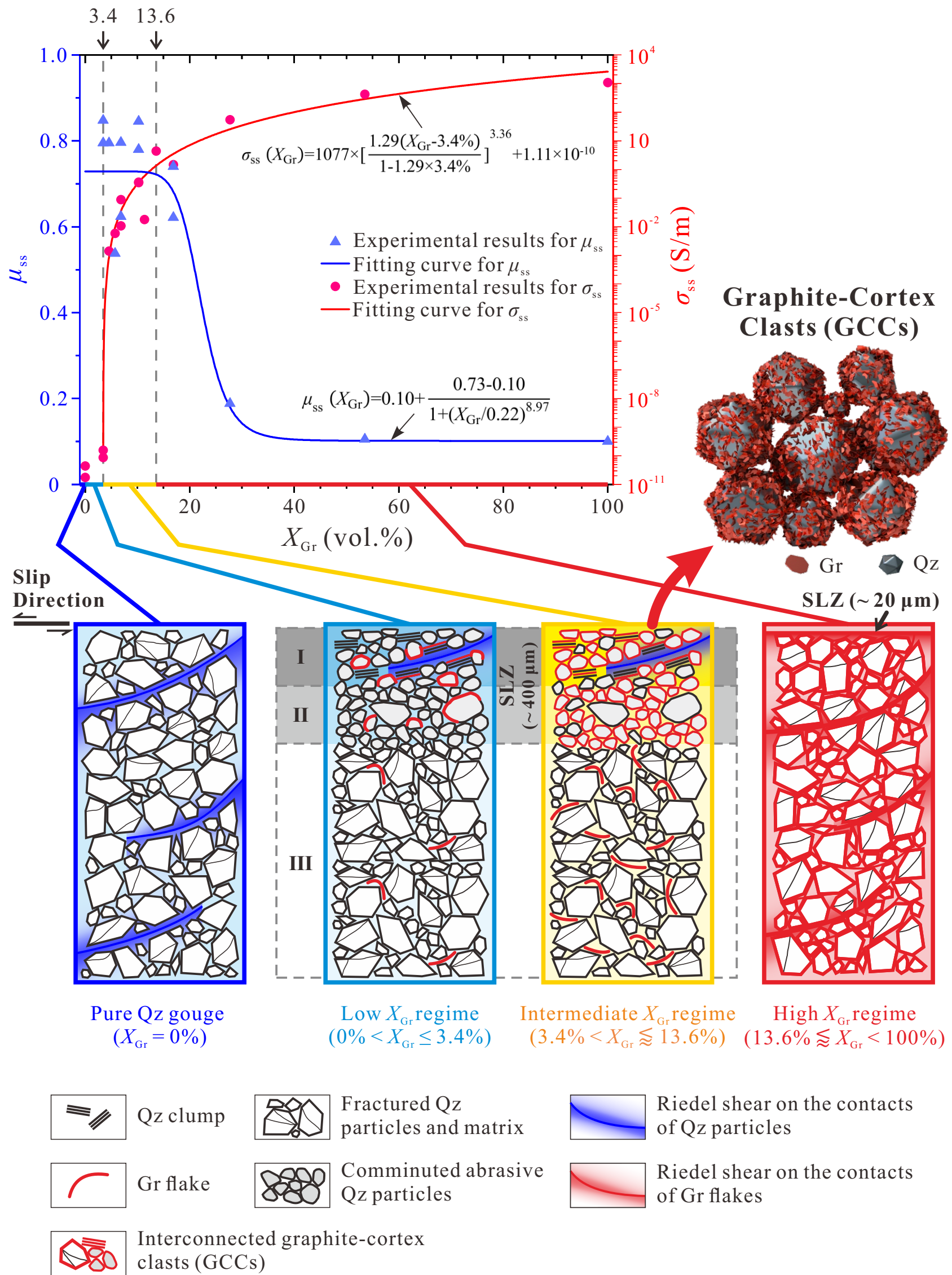


Figure 8.

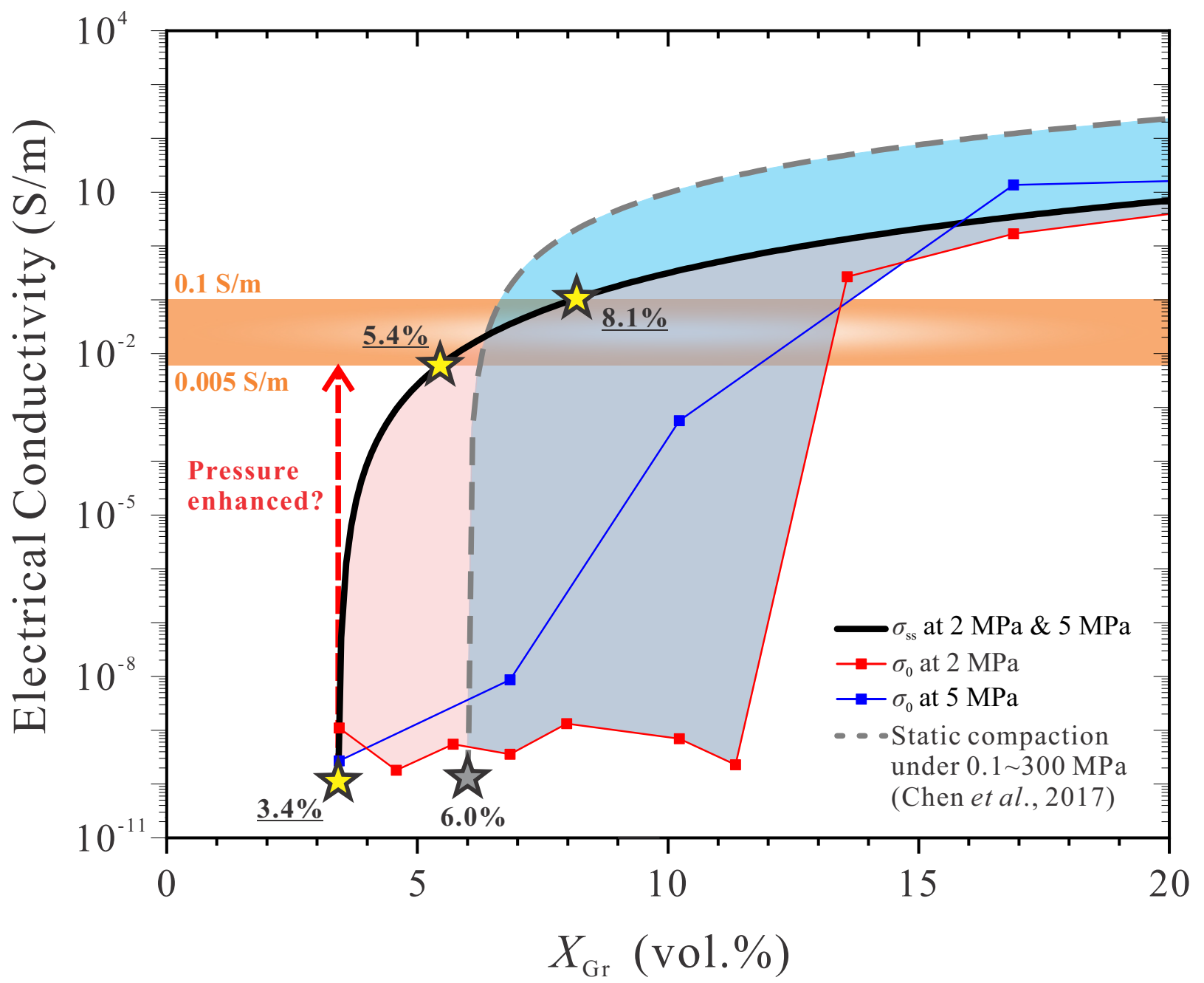
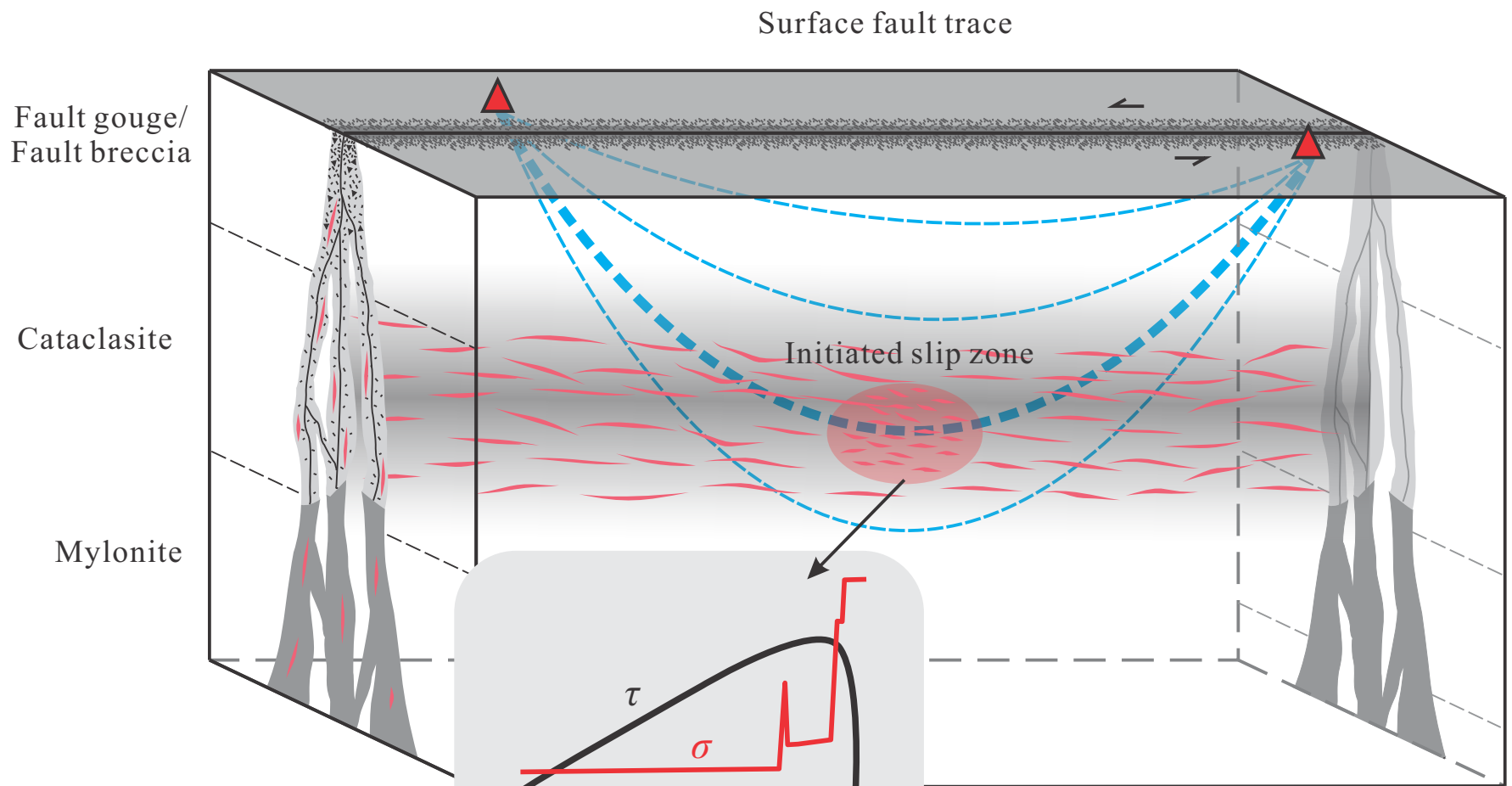


Figure 9.




 Electrical resistivity station


 Electrical current pathways of varied frequency bands


 Gr-bearing shear zone